NASA Contractor Report 198442

Oscillating-Flow Regenerator Test Rig: Hardware and Theory With Derived Correlations for Screens and Felts

D. Gedeon
Gedeon Associates
Athens, Ohio

and

J.G. Wood
Wood Experimental
Albany, Ohio

February 1996

Prepared for
Lewis Research Center
Under Grant NAG3–1269

National Aeronautics and
Space Administration

Contents

Summary

A number of wire mesh and metal felt test samples, with a range of porosities, yield generic correlations for friction factor, Nusselt number, enhanced axial conduction ratio and overall heat flux ratio. This information is directed primarily toward stirling-cycle regenerator modelers, but will be of use to anyone seeking to better model fluid flow through these porous materials.

Behind these results lies an oscillating-flow test rig, which measures pumping dissipation and thermal energy transport in sample matrices, and several stages of data-reduction software, which correlate instantaneous values for the above dimensionless groups. Within the software, a theoretical model reduces instantaneous quantities from cycle-averaged measurables using standard parameter estimation techniques.

Chapter 1

Introduction

1.1 The Continuing Saga

This report is actually the fourth in a series of reports on progress milestones for this regenerator test rig. A 1989 report [3] covered test-rig design and data-reduction methodology, but no actual testing, under a NASA Lewis SBIR (Small Business Innovative Research) contract to Sunpower Incorporated. The hardware has been considerably revised since then but the data-reduction methodology remains about the same. A 1992 report [4] presented preliminary pressure-drop and heat-transfer correlations for a few woven-screen and metal-felt matrices under the auspices of a NASA grant to the Ohio University Center for Stirling Technology Research (CSTR). And a 1994 report [13] summarized a larger number of tests, run but not yet completely reduced, as the conclusion to the test program under the now defunct CSTR.

In this report, all of the previously-reported screen and felt experimental data have been reduced into generic correlations intended for application to all woven-screen matrices or all metal-felt matrices. This final step was made possible through NASA service-contract funding to Gedeon Associates. We have also made some effort to make this report reasonably self-contained by including a description of the hardware, theory and software in several appendices. One exception to this is the matter of error analysis, the theory of which seemed too lengthy and convoluted to reproduce here. While this report mentions various computed error estimates, it does not deal much with the theory behind them. Interested readers will have to refer to the original 1989 report [3] for the theoretical details.

1.2 Samples Tested

We tested a total of seven matrices, three woven-screen type and four metal-felt type. All samples are representative of regenerator matrices used in stirling machines:

200 mesh 200 mesh (per inch) stainless steel woven wire screens, sintered, wire diameter 53.3 microns (0.0021 in), porosity 0.6232, sample thickness 10.1 mm

100 mesh 100 mesh (per inch) stainless steel woven wire screens, stacked, wire diameter 55.9 microns (0.0022 in), porosity 0.7810, sample thickness 17.5 mm

80 mesh 80 mesh (per inch) stainless steel woven wire screens, stacked, wire diameter 94.0 microns (0.0037 in), porosity 0.7102, sample thickness 22.1 mm

2 mil felt inconel metal felt, round wire 50.8 micron (0.002 in) diameter, porosity 0.688, sample thickness 7.54 mm

1.5 mil felt (top sample) stainless steel metal felt, round wire 38.1 micron (0.0015 in) diameter, porosity 0.730, sample thickness 7.67 mm

1.5 mil felt (middle sample) same material, porosity 0.748, sample thickness 7.49 mm

1 mil felt stainless steel metal felt, round wire 25.4 micron (0.001 in) diameter, porosity 0.8200, sample thickness 12.7 mm

0.5 mil felt stainless steel metal felt, round wire 12.7 micron (0.0005 in) diameter, porosity 0.8405, sample thickness 14.9 mm

The metal-felt matrices were all manufactured by the Technetics (metal fiber) division of the Brunswick Corporation, which has since been re-organized into Memtec America Corporation, Fluid Dynamics Division, Deland FL, (904) 822-8000. Memtec continues to produce fine-gauge drawn wires of round (or nearly round) cross section and sintered metal felts made from these wires. These felts have a random fiber orientation with the fibers lying predominantly transverse to the flow direction. The samples labeled *top* and *middle* were respectively cut from the top and middle regions of a single regenerator matrix in order to evaluate any difference due to manufacturing process. Evidently there is a small difference in porosity, probably due to the portion near the middle being somewhat shielded from the metal rollers used to compress the sample to its nominal thickness. A micrograph of a typical metal-felt matrix appears in figure 1.1.

The screen matrices were all assembled in-house by stacking together individual layers in random orientation. Only one of the above samples was sintered because the previous report [4] concluded that there was no significant difference in heat-transfer or pressure-drop characteristics produced by sintering compared to cold stacking. In either case though, there is some variability in packing density for the final matrix assembly, depending on the pressure exerted to compress the layers. Our procedure involved pressing layers together between lathe centers to achieve a desired porosity. Quoted porosity is overall-matrix porosity

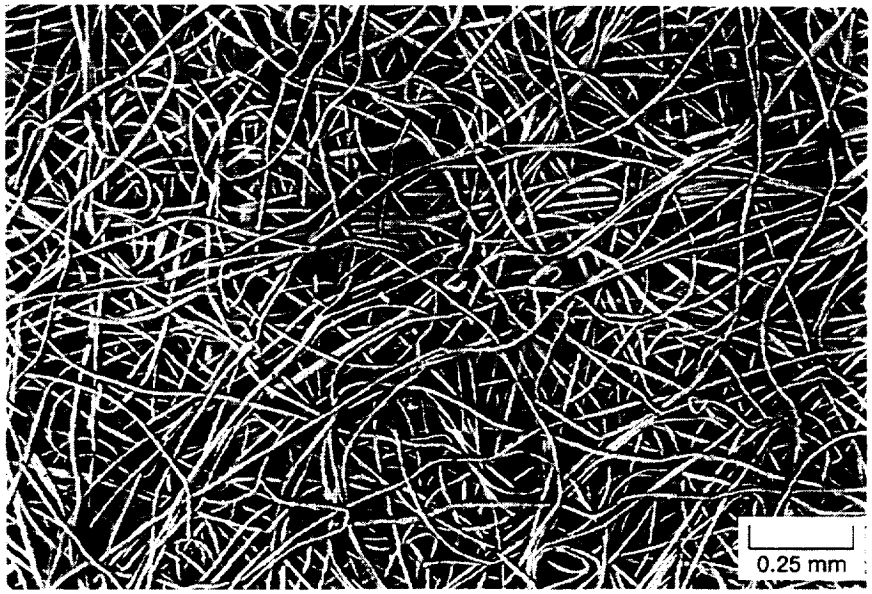

Figure 1.1: Micrograph of a metal-felt matrix magnified 50×.

rather than ideal single-screen porosity. A source for woven screens is Cleveland Wire Cloth, Cleveland OH, (216) 341-1832. A micrograph of a typical woven-screen matrix appears in figure 1.2.

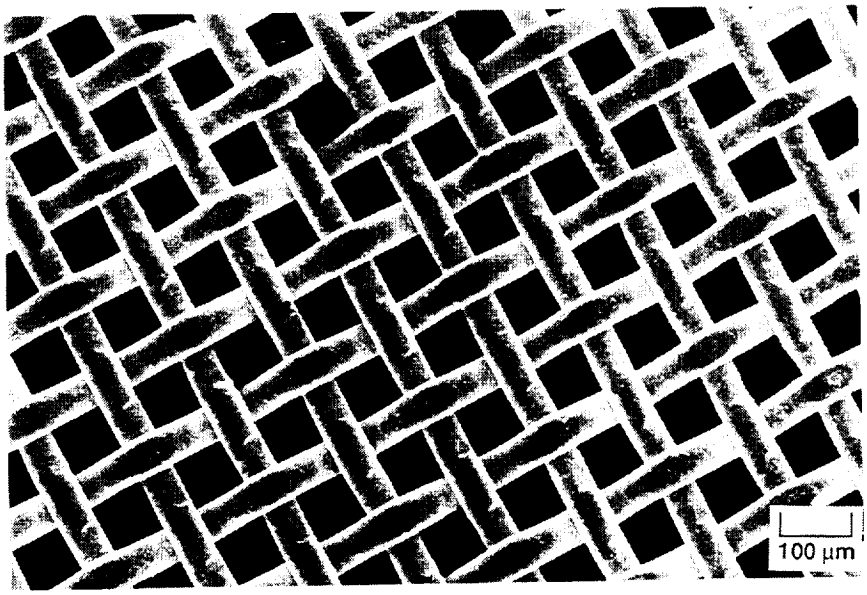

Figure 1.2: Micrograph of a woven-screen matrix magnified 100×.

Chapter 2

Screen and Felt Correlations

Presented here are correlating expressions, derived from test data, for regenerator pressure-drop and heat transfer in terms of mean flow variables available in simulation models or from experimental measurement. Symbols are defined in appendix A. Details of testing and data reduction are the topic of the next section.

Although all samples were metallic (usually stainless steel) there is nothing preventing these correlations from applying to non-metallic matrices of similar structure. Polyester-fiber felts, in particular, are sometimes used as stirling-cooler regenerator matrices and are likely to be structurally identical to metal felts. The validity of this assertion rests on the fact that flow friction, heat transfer and enhanced axial conduction are all phenomena that occur solely within the gas as it flows around the solid obstructions of the matrix. Solid conduction and specific heat are independent phenomena whose affect on our final correlations was judged to be negligible over the experimental conditions encountered. Even when solid phenomena are significant (below 10 K, for example, when heat capacity drops off), they are properly modeled within the solid itself and not within the gas. Physically, the matrix solid can only affect the surface temperature seen by the gas, and the gas sees that surface temperature just like any other.

2.1 Darcy Friction Factors

We started out modeling friction factors in the standard two-parameter Ergun form [9]

$$f = a_1/R_e + a_2 \tag{2.1}$$

where a_1 and a_2 were to be determined. However, we were able to get a much better fit to data by introducing a relatively minor modification to the Ergun

equation. We call this the three-parameter modified-Ergun form:

$$f = a_1/R_e + a_2 R_e^{a_3} \tag{2.2}$$

The idea is that parameter a_3 will be negative but small, allowing the correlation to better track observed reality at high R_e. At low R_e (creeping viscous flow) the a_1/R_e will dominate, exactly as in the original Ergun equation.

Estimated parameters a_1, a_2 and a_3 appear in the following tables for the various matrices tested:

Woven Screens

	200 mesh	100 mesh	80 mesh
a_1	129.3 ± 0.3	138.9 ± 0.5	120.1 ± 0.5
a_2	2.990 ± 0.038	2.567 ± 0.020	2.369 ± 0.020
a_3	-0.0758 ± 0.0019	-0.0816 ± 0.0010	-0.0836 ± 0.0010
R_{em} range	0.45 — 1700	0.88 — 5200	2.2 — 6100
V_a range	0.0052 — 3.0	0.026 — 17	0.042 — 21
δ/L range	0.028 — 2.2	0.087 — 1.2	0.079 — 0.95

$\pm$ values are 90% confidence intervals (*see* appendix D)

Metal Felts

	2.0 mil	1.5 mil (top)	1.5 mil (mid)
a_1	120.7 ± 0.5	214.1 ± 0.6	239.1 ± 0.7
a_2	3.730 ± 0.033	6.629 ± 0.068	8.295 ± 0.071
a_3	-0.0627 ± 0.0013	-0.0703 ± 0.0016	-0.0903 ± 0.0013
R_{em} range	0.83 — 2500	0.67 — 1500	0.36 — 1800
V_a range	0.015 — 5.2	0.012 — 3.7	0.005 — 5.6
δ/L range	0.19 — 2.6	0.19 — 2.4	0.15 — 2.6
	1 mil	0.5 mil	
a_1	213.8 ± 0.5	211.6 ± 0.7	
a_2	4.514 ± 0.041	4.217 ± 0.064	
a_3	-0.0705 ± 0.0014	-0.0651 ± 0.0024	
R_{em} range	0.21 — 1800	0.11 — 900	
V_a range	0.0056 — 5.3	0.0021 — 1.6	
δ/L range	0.043 — 1.3	0.102 — 2.2	

$\pm$ values are 90% confidence intervals

We had hoped to combine the above results into two master correlations — one for all screens and one for all felts — by introducing a porosity dependence into the modified Ergun equation. The correlating expression was to be the four-parameter form

$$f = (a_1/R_e + a_2 R_e^{a_3})\,\beta^{a_4} \tag{2.3}$$

where β is porosity. Unfortunately this expression did not seem to fit the data very well. As judged by plots of modeling residuals, the fit was only marginally better than the above three-parameter expression, applied to the combined screens or combined felt data. The reason must have had to do with

variations in the individual samples not correlated with porosity — structural dissimilarities at a microscopic level, for example. Even without explicit porosity dependence, porosity does affect the calculation of hydraulic diameter d_h and void-average flow velocity u, in terms of which friction factor is defined. This seems to be as much porosity dependence as our data justifies.

So, the best we were able to do was apply the three-parameter friction factor to the combined data sets of all screens and all felts. In doing so we lost a good deal of our precision of fit to the data. Reduced individually, worst-case residuals (deviations of data from model as a fraction of estimated random error) were on the order of ± 5. Reduced together, worst-case residuals were on the order of ± 30 for screens and ± 80 for felts (*see* figure 3.1). Were it not for the extremely high signal to noise ratio of about 300 (*see* figure 3.2), this would be bad news indeed. As it is, it suggests a worst-case relative pressure drop error of about 27% for felts and 10% for screens when applying the following combined correlations to a generic woven-screen or metal-felt matrix (*see* section 3.1):

Woven Screens

$$f = 129/R_e + 2.91 R_e^{-0.103} \tag{2.4}$$

Metal Felts

$$f = 192/R_e + 4.53 R_e^{-0.067} \tag{2.5}$$

Or in tabular form:

	Woven Screens	Metal Felts
a_1	129.3 ± 0.2	192.4 ± 0.2
a_2	2.913 ± 0.013	4.533 ± 0.020
a_3	-0.1027 ± 0.0006	-0.0672 ± 0.0007
R_{em} range	0.45 — 6100	0.11 — 2500
V_a range	0.0052 — 21	0.0021 — 5.6
δ/L range	0.028 — 2.2	0.043 — 2.6

± values are 90% confidence intervals

The above correlations are plotted in figures 2.1 and 2.2.

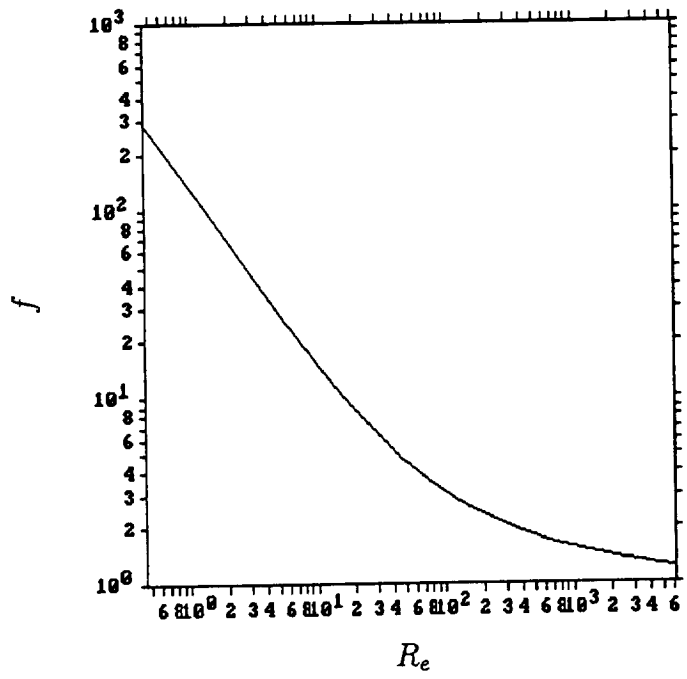

Figure 2.1: Oscillating-flow friction factor for the combined woven screen test samples

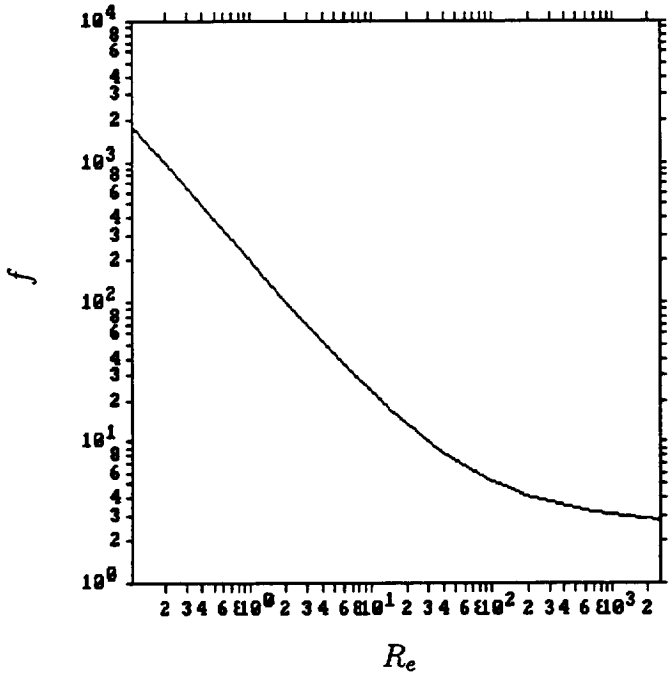

Figure 2.2: Oscillating-flow friction factor for the combined metal felt test samples

2.2 N_u and N_k Simultaneously

Nusselt numbers and enhanced conductivity ratios as presented here should be used together in an oscillating-flow regenerator model that simultaneously includes the effects of both film heat transfer and enhanced axial conduction. Since they are based on best estimates of the true regenerator physics, they may also be used with caution by porous flow modelers in other fields. See appendices C and F for further discussions on the nature and use of N_u and N_k.

Results for the individual woven-screen and metal-felt samples are not presented since, this time, we were more successful in combining data sets to produce two master correlations — one for all screens and one for all felts. The likely reason for our success is that porosity has a fundamental physical affect on Nusselt number N_u and axial conductivity ratio N_k that overwhelms any structural variations.

The presumed correlating expressions are in terms of Peclet number (R_eP_r) and porosity:

$$N_u = (1 + a_1 P_e^{a_2})\beta^{a_3} \tag{2.6}$$

$$N_k - N_{k0} = a_4 P_e^{a_2} \beta^{a_5} \tag{2.7}$$

The constant 1 in the Nusselt number expression is a concession to prevent N_u from vanishing for $P_e = 0$, which may be important in preventing thermal decoupling of the gas and matrix, and possible instability, in numerical simulations. It is small enough not to significantly affect our parameter estimation. Some constant value is justified by laminar solutions in simple geometries, where N_u tends to some fixed non-zero value N_{u0} as P_e approaches zero. A value of $N_{u0} \approx 1$ seems reasonable in light of the published limiting value of $hd_w/k = 0.43$ (Nusselt number based on wire diameter) in [6] for flow normal to a single cylinder. The definition of N_u employed in the present report is based on hydraulic diameter and is a factor of $\beta/(1-\beta)$ larger. Unfortunately, due to the dominance of enhanced conduction as the axial energy transport mechanism for low P_e's, it is not possible to estimate N_{u0} directly from our data.

That the P_e exponents for both N_u and N_k are the same reflects the assumption that the underlying enhancement mechanisms are the same for both. In essence, the argument is that fluctuating parts of velocity and temperature fields enhance axial thermal diffusion by the same factor they enhance gas-to-matrix heat transfer. This topic is picked up again in appendix F. It would be nicer if we didn't have to make this assumption but previous efforts have shown that it is impossible to independently correlate P_e dependence for both N_u and N_k from our data.

On the other hand, it does turn out to be possible to independently correlate porosity dependence for N_u and N_k. Based on considerations presented below, it is arguable that the asymptotic form for Nusselt number as $\beta \rightarrow 1$ should scale as $\beta/(1-\beta)$, raised to some positive exponent while the asymptotic form for enhanced axial conductivity should do likewise, except for a negative exponent. But when we tried correlating N_u and N_k in terms of $(\beta/(1-\beta))^a$ or even

$(1-\beta)^a$, (exponents a different for N_u and N_k) we found the fit to the data, as measured by the residuals, was significantly worse than when correlated in terms of β^a. Evidently, our porosities were never high enough for the asymptotic behavior to kick in? Highest porosities tested were 0.78 for screens and 0.84 for felts. So, on empirical grounds we must say that over the limited range of porosities represented in our samples, a porosity dependence in the form β^a appears to fit the data best.

Final correlating expressions for the two types of material are:

Woven Screens

$$N_u = (1+0.99P_e^{0.66})\beta^{1.79} \quad (2.8)$$

$$N_k - N_{k0} = 0.50P_e^{0.66}\beta^{-2.91} \quad (2.9)$$

Metal Felts

$$N_u = (1+1.16P_e^{0.66})\beta^{2.61} \quad (2.10)$$

$$N_k - N_{k0} = 1.30P_e^{0.66}\beta^{-2.09} \quad (2.11)$$

Or in tabular form:

	Woven Screens	Metal Felts
a_1	0.991 ± 0.048	1.159 ± 0.033
a_2	0.662 ± 0.005	0.656 ± 0.005
a_3	1.792 ± 0.048	2.609 ± 0.049
a_4	0.504 ± 0.12	1.299 ± 0.090
a_5	-2.908 ± 0.48	-2.089 ± 0.24
R_{em} range	1.04 — 3400	0.79 — 1400
V_a range	0.0048 — 16	0.0037 — 3.3
δ/L range	0.17 — 3.0	0.17 — 3.8

$\pm$ values are 90% confidence intervals

The above correlations are plotted in figures 2.3 and 2.4 and residuals are plotted in figure 3.3.

One cannot help but notice the strong dependence of both N_u and N_k on porosity and that N_u increases with porosity while N_k decreases. That the dependence is strong is tempered by the observation that porosity typically only varies over the range of about 0.60 to 0.90 in most regenerators. Even the strongest porosity factors in the above correlations vary only by a factor of about 3 over this range. Perhaps more interesting are the trends of the correlations. These are at least in the correct direction, which we can deduce by arguing about the high-porosity limiting case where the matrix looks like empty space with a few widely scattered wires. For then, Nusselt number (based on hydraulic diameter) will tend to the value for a single cylinder in cross flow, which has already been remarked to scale by the ratio of hydraulic diameter to wire diameter, or $\beta/(1-\beta)$, which increases as β increases. This is somewhat countered by the Reynolds number dependence of single-cylinder Nusselt number which

scales roughly as $R_{e_w}^{0.5}$ over the range of interest, where R_{e_w} is Reynolds number based on wire diameter, rather than hydraulic diameter. When cast in terms of our Peclet number this introduces a factor $(\beta/(1-\beta))^{-0.5}$ into N_u, enough to reduce but not overwhelm the previous factor. In the case of enhanced axial conductivity, we expect R_{e_w} to again characterize the flow in the limit $\beta \to 1$ so that N_k should also scale roughly as $R_{e_w}^{0.5}$. We might also throw in a factor of $(1-\beta)/\beta$, the filled-to-void volume ratio, to account for the fraction of the volume filled by turbulent wakes. Based on these considerations, we expect a porosity dependence of roughly $((1-\beta)/\beta)^{1.5}$ in our N_k expression, which decreases as β increases.

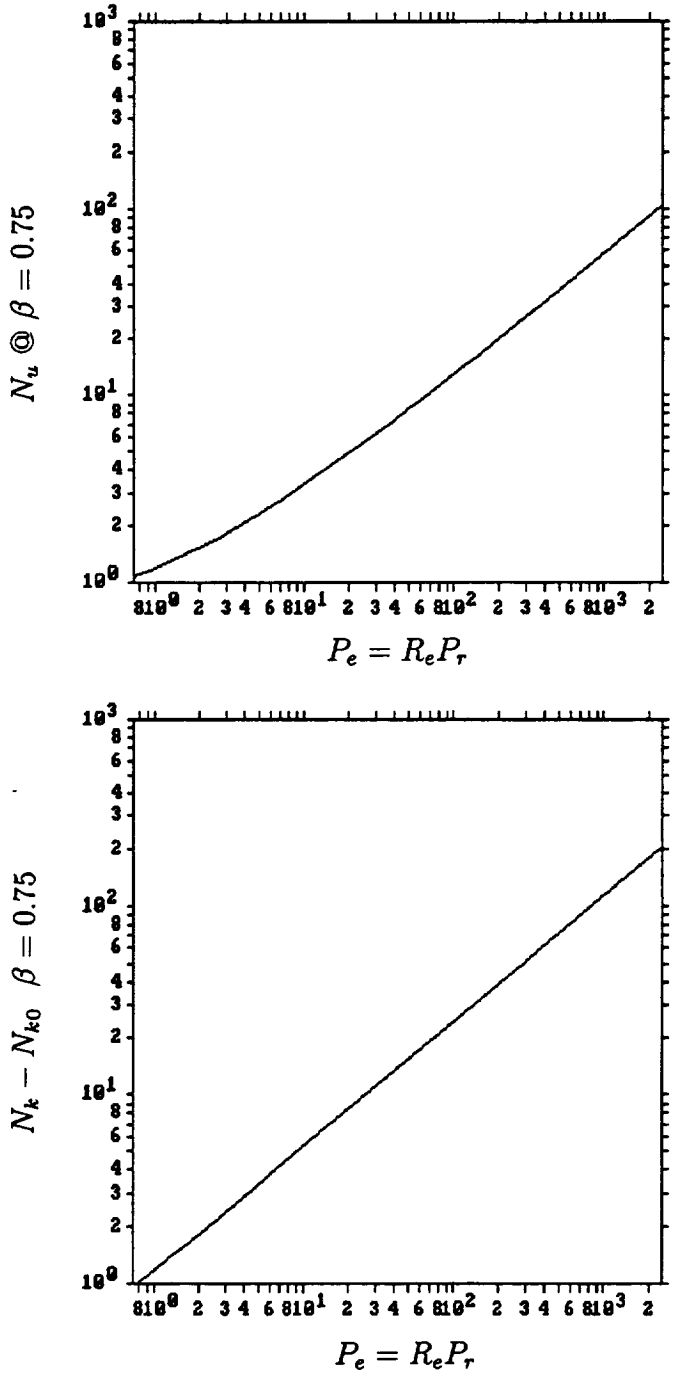

Figure 2.3: Oscillating-flow Nusselt number and enhanced axial conductivity ratio for woven screen, for $\beta = 0.75$

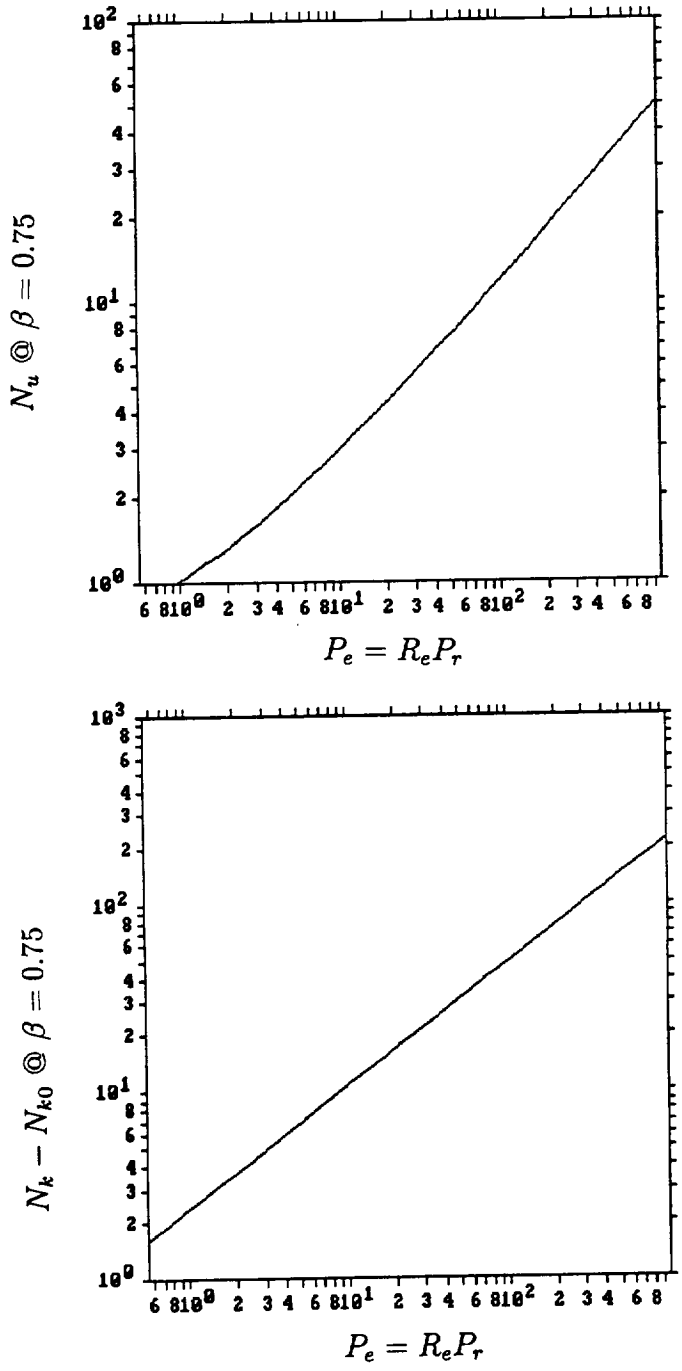

Figure 2.4: Oscillating-flow Nusselt number and enhanced axial conductivity ratio for metal felt, for $\beta = 0.75$

2.3 N_{ue} assuming $N_k = N_{k0}$

Effective Nusselt number N_{ue} captures the total oscillating-flow regenerator heat flux q_i^* in enthalpy transport alone. We intended it for use primarily by stirling modelers who prefer to neglect enhanced axial conduction. In other applications it will tend to under-predict actual film heat transfer for a given temperature difference — especially at Peclet numbers below about 10. The presumed correlating expressions are

$$N_{ue} = (1 + a_1 P_e^{a_2})\beta^{a_3} \quad (2.12)$$

$$N_k - N_{k0} = 0 \quad (2.13)$$

The constant 1 in the Nusselt number expression and the form of the porosity dependence are there for the same reasons as previously discussed for simultaneous N_u, N_k modeling.

Final correlating expressions for the two types of material are:

Woven Screens

$$N_{ue} = (1 + 0.64 P_e^{0.72})\beta^{1.79} \quad (2.14)$$

Metal Felts

$$N_{ue} = (1 + 0.48 P_e^{0.79})\beta^{2.75} \quad (2.15)$$

Or in tabular form:

	Woven Screens	Metal Felts
a_1	0.644 ± 0.017	0.485 ± 0.007
a_2	0.720 ± 0.003	0.794 ± 0.002
a_3	1.794 ± 0.030	2.752 ± 0.028
R_{em} range	1.04 — 3400	0.79 — 1400
V_a range	0.0048 — 16	0.0037 — 3.3
δ/L range	0.17 — 3.0	0.17 — 3.8

$\pm$ values are 90% confidence intervals

The above correlations are plotted in figures 2.5 and 2.6 and residuals are plotted in figure 3.4. The narrower confidence bands this time reflect the comparative ease of modeling three rather than five parameters, not any intrinsic superiority of the world view neglecting enhanced axial conduction. In fact, the previous five-parameter modeling for simultaneous N_u and N_k gave a slightly but significantly better fit to the data, as measured by the minimum chi-squared value of the residuals.

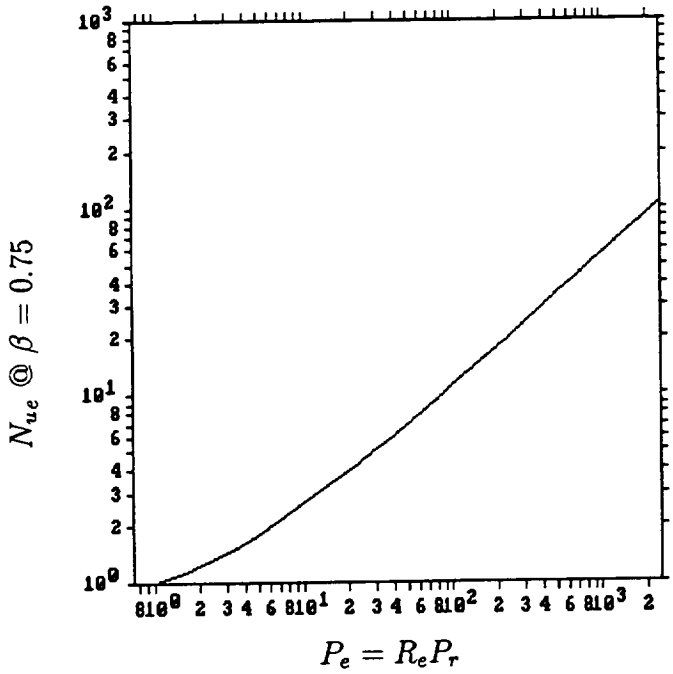

Figure 2.5: Effective Nusselt numbers neglecting enhanced axial conduction, for woven screen, for $\beta = 0.75$

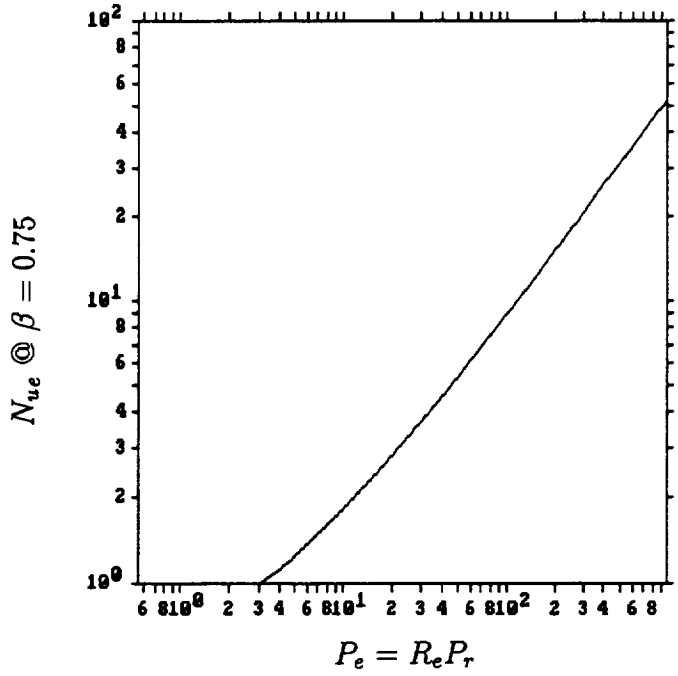

Figure 2.6: Effective Nusselt numbers neglecting enhanced axial conduction, for metal felt, for $\beta = 0.75$

2.4 Overall Heat Flux Ratios

Overall heat flux ratio correlates the overall thermal loss down an oscillating-flow regenerator with a simple expression in terms of the peak Peclet number and porosity.

$$N_q = a_1 P_{em}^{a_2} \beta^{a_3}$$

Note that Peclet number is the *peak* not instantaneous value. As judged by the minimum chi-squared value of the residuals (figure 3.5), this expression does not fit the data as well as the previous expression for N_u and N_k, but somewhat better than the expressions for N_{ue}. This is a rather remarkable achievement for such a simple idea.

Final correlating expressions for the two types of material are:

Woven Screens

$$N_q = 0.194 P_{em}^{1.30} \beta^{-1.81} \tag{2.16}$$

Metal Felts

$$N_q = 0.253 P_{em}^{1.24} \beta^{-2.67} \tag{2.17}$$

Or in tabular form:

	Woven Screens	**Metal Felts**
a_1	0.194 ± 0.005	0.253 ± 0.003
a_2	1.301 ± 0.003	1.239 ± 0.002
a_3	-1.806 ± 0.030	-2.672 ± 0.029
R_{em} range	1.04 — 3400	0.79 — 1400
V_a range	0.0048 — 16	0.0037 — 3.3
δ/L range	0.17 — 3.0	0.17 — 3.8

$\pm$ values are 90% confidence intervals

The above correlations are plotted in figures 2.7 and 2.8 and residuals are plotted in figure 3.5.

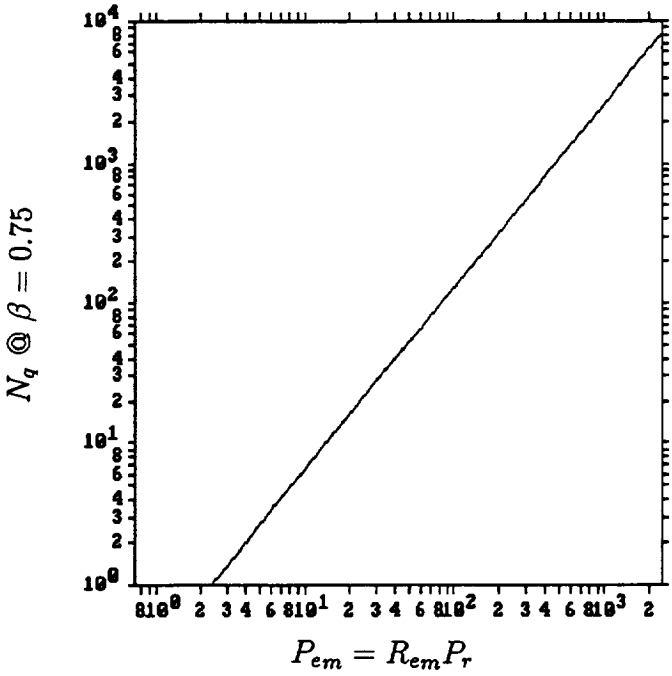

Figure 2.7: Overall heat flux ratios for woven screen, for $\beta = 0.75$

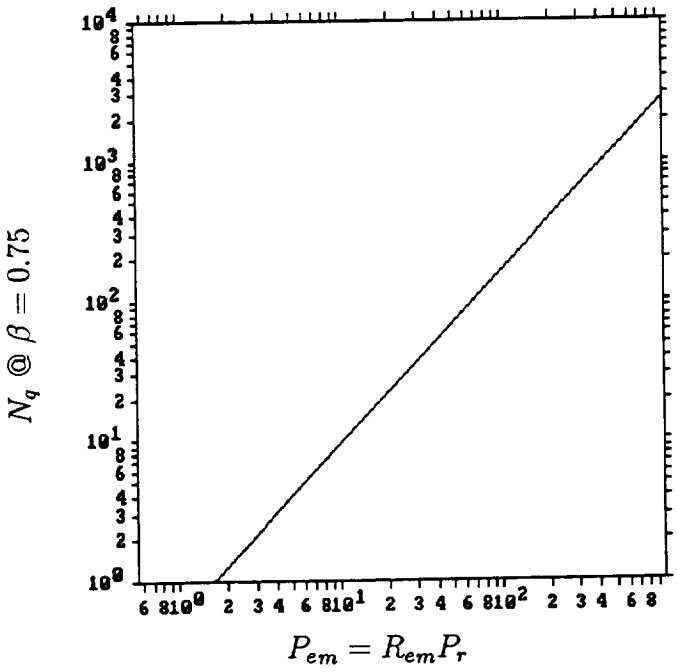

Figure 2.8: Overall heat flux ratios for metal felt, for $\beta = 0.75$

Chapter 3

Test Details

3.1 Pressure-Drop Tests

Pressure-drop testing is relatively straight forward, involving only a measurement of sample pumping dissipation inferred from the PV work done by the piston. The principal uncertainties are due to the compressibility of the working gas when pressure-drop is large.

3.1.1 Data Sets

Individual samples were tested as follows:

Pressure Drop Tests

	test dates	no. points
200 mesh screens	11-03-92	169
100 mesh screens	11-04-92, 11-05-92	237
80 mesh screens	11-02-92	193
2.0 mil felt:	6-29-93	176
1.5 mil felt (top)	6-30-93	148
1.5 mil felt (mid)	6-02-93	159
1.0 mil felt	11-04-92	201
0.5 mil felt	11-03-92	168

Derived data for all screens were collected into file PSCN.DRV and for all felts into PFELT.DRV as the basis for the final correlations in this report.

3.1.2 Error Analysis

In data modeling parlance, residuals measure the fit of our model to the experimental data and show the nature of any discrepancy between the two. This information cannot be directly plotted on our friction factor curves because our experimental *measurable* is not instantaneous pressure drop but, rather, cycle-mean sample pumping dissipation. So we need separate residual plots, which

the data modeling software produces each time it runs. Plotted residuals are normalized by the estimated random measurement errors, which in this case are the random errors expected in calculating cycle-mean pumping dissipation, a quantity derived for each data point in terms of position and pressure transducer errors. The data modeling software also produces plots of signal-to-noise ratio, which in this case show the actual values of measured cycle-mean pumping dissipation, normalized by the same estimated random measurement errors.

Residual plots for our master *screen* and *felt* friction factors are shown in figure 3.1. Ideally, residuals should fall randomly between $\pm$ 1, when the data fit the model. With actual residuals falling in the range $\pm$ 30 for screens and $\pm$ 80 for felts, this is decidedly not the case. This can mean one of two things: Either the model is bad or the random error is so small that even a small discrepancy in the model shows up as a large residual error. In the present case the latter phenomenon appears largely responsible. The two measurements that contribute to random measurement error are time-varying piston position and pressure. Estimated measurement errors for these were 36 microns (0.0014 in) and 2.8 Pa (0.0004 psi), respectively — remarkably small. These estimates were verified by analysis of data on a relatively small test sample. Remember that the errors we are talking about here are the random errors produced by two separate readings of the same piston position and pressure, rather than the systematic error, in absolute terms, due to mis-calibration or whatever. The true impact of these small errors may be seen in the plot of signal-to-noise ratios in figure 3.2 which range up to about 300 for both screens and felts. A residual of 80, presuming it corresponds to a high-signal data point, is therefore only about $80/300 = 0.27$ of the total signal while a residual of 30 is only about 0.10 of the signal. And these are worst-case errors. From this we can expect our correlations to predict pressure drop within about 27% for felts and 10% for screens, at worst. Agreement will probably be better for most cases.

Although not shown, residuals for individual-sample friction factors are much lower. In fact they fall in the range of ± 5, indicating a much better fit of data to model.

One additional source of error worth considering in pressure drop testing is the error in the model-predicted pumping dissipation as a result of variations in mass flux g across the test sample. Mass flux varies because of time-dependent density variations resulting from the pressure swing in the cylinder volume. The pressure-drop data modeling software produces an error plot which estimates the relative magnitude of this error. This error was small for all samples tested.

3.1.3 Comparison to Other Data

Published data for friction factors in steady porous flow is relatively common. Oscillating-flow results are much rarer, but this does not worry us too much because of the negligible role Valensi number (measure of dimensionless frequency) seems to play in our data, as was demonstrated in [4].

For comparison purposes we used results reported for screens in figure 7-9, p. 149, of Kays and London [7]. Because of the lack of an analytic formulation

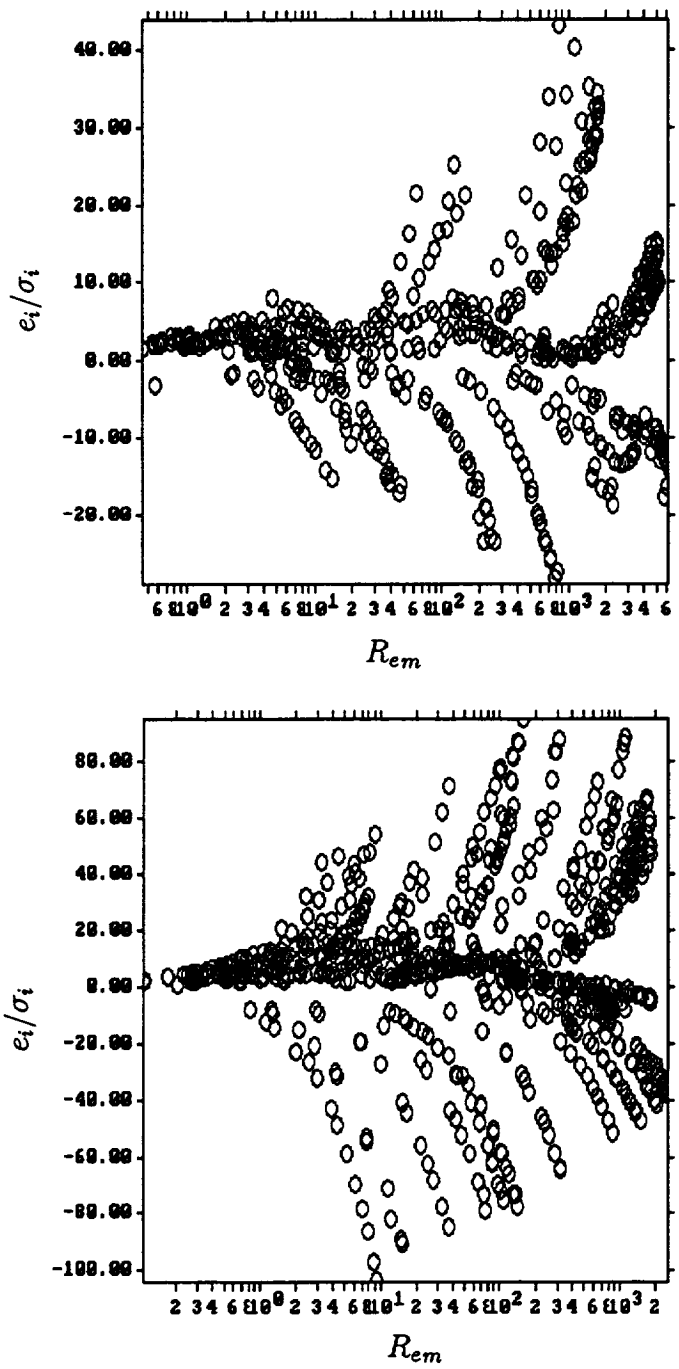

Figure 3.1: Residuals for modified-Ergun friction-factor parameter estimates: combined woven screens χ^2 = 7.22E4 with 599 points (top), combined metal felts χ^2 = 8.62E5 with 852 points (bottom).

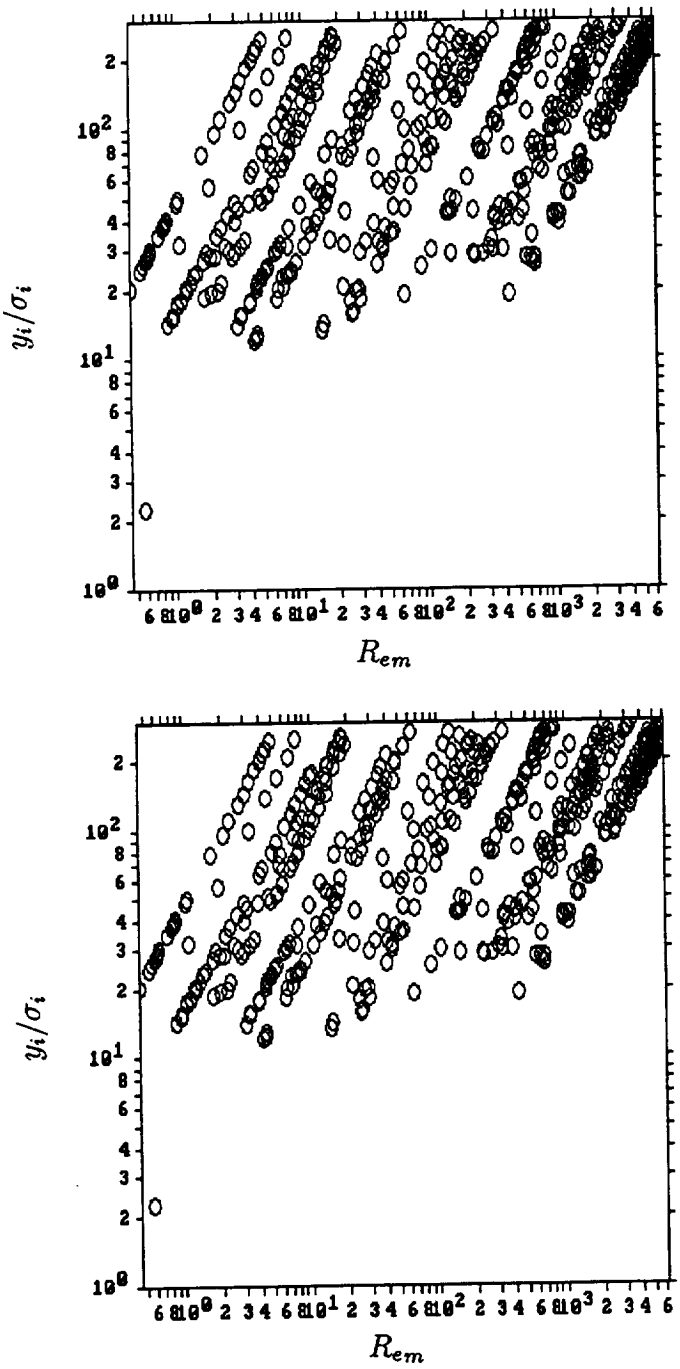

Figure 3.2: Signal to noise ratios for friction-factor parameter estimates: combined woven screens (top), combined metal felts (bottom).

for the Kays and London data, we have not plotted a comparison of our woven-screen friction factor against theirs. Rather, we have tabulated the agreement at several representative Reynolds numbers. When comparing our Darcy friction factors to Kays and London's Fanning factors we must always remember to multiply by 4.

Screen Friction Factor Comparison

R_e	8	40	100	400	1000	6000
f — low Kays & London	18	5.2	3.0	1.8	1.4	1.1
f — present report	18.5	5.21	3.10	1.89	1.56	1.40
f — high Kays & London	29	8.5	4.5	2.7	2.1	1.6

The table covers a Reynolds number range from 8 to 6000, which was the range of overlap for our respective data sets. Peak Reynolds number for our experiments ranged from 0.45 to 6100, while Kays and London steady Reynolds numbers ranged from 8 to 10^5. It is seen that our woven-screen friction factor falls on the low side of the Kays and London data for low Reynolds number while near the middle for high Reynolds numbers. The Kays and London data was based on four discrete porosities: 0.832, 0.766, 0.725, 0.602, with either 0.832 or 0.602 (depending on R_e) producing the *high* friction factor and 0.725 producing the *low* friction factor. Interestingly, their data, like ours, shows no clear trend with porosity. And, there is about a $\pm$ 25% scatter among their four samples, in the ballpark of our $\pm$ 10% accuracy projections based on relative pumping-dissipation error.

The Kays and London correlations were "established from tests of wire screens at the low Reynolds number end but crossed-rod matrices at the high Reynolds number end", as they explain it. Data for screens alone was reported in Coppage and London [2] for Reynolds numbers up to about 1000 and the same porosities appearing in Kays and London [7]. Apparently, the Coppage and London data were combined with later crossed-rod data to produce the Kays and London correlations. But, the structure of a crossed-rod matrix (comprised of straight rods) is noticeably different than a true woven screen; a fact that should be kept in mind when comparing our data to theirs.

3.2 Heat-Transfer Tests

As its principal experimental variable, heat transfer testing measures net heat flux down the regenerator inferred from cooler heat rejection less PV power and heat leaks. Compared to pressure-drop testing, this is more complicated, time consuming, and noisier; the noise being chiefly due to the rather large and time-varying nature of heat leakage.

3.2.1 Data Sets

Individual samples were tested as follows:

Heat Transfer Tests

	test dates	no. points
200 mesh screens	11-17-92, 11-18-92	273
100 mesh screens	11-16-92, 11-17-92	231
80 mesh screens	11-12-92	189
2.0 mil felt:	11-21-92, 11-22-92	227
1.5 mil felt (top)	11-23-92	272
1.5 mil felt (mid)	3-10-93, 3-11-93	283
1.0 mil felt	11-18-92, 11-19-92	286
0.5 mil felt	10-07-92, ..., 10-12-92	271

Derived data for all screens were collected into file HSCN.DRV and for all felts into HFELT.DRV as the basis for the final correlations in this report.

3.2.2 Error Analysis

For our heat-transfer tests we have three sets of residuals corresponding to the simultaneous N_u and N_k modeling, N_{ue} modeling or N_q modeling. In all cases the measured experimental variable is cycle average heat flux down the matrix, less static thermal conduction, and the normalization error is the random component of this, calculated for each data point in terms of various transducer errors. The theoretical experimental variable varies though, depending on which model is being compared to the data.

The various residuals are plotted in figures 3.3, 3.4 and 3.5. Compared to the friction-factor residuals, these residuals are much smaller, falling in the range of $\pm$ 4 for both screens and felts, suggesting a better fit to the data, or higher noise since the signal-to-noise ratios in figure 3.6 range only to about 40. By comparing normalized residuals to signal-to-noise ratios at various Reynolds numbers, we are led to expect a prediction of overall regenerator energy flux to within $\pm$ 10% near the high-end of the Reynolds number range with accuracy falling off for lower Reynolds numbers to no better than $\pm$ 50% below Reynolds number about 5, using any of our correlations. Another feature of the heat-transfer residuals compared to the friction-factor residuals is that they are more randomly distributed, showing hardly any systematic deviations from the model. This suggests the residuals are indeed produced by random measurement errors, as they are supposed to be, even though these errors may be relatively large.

The heat-transfer data modeling software also produces a number of other error plots, namely

1. Relative error induced by g error
2. Relative error induced by T error
3. Relative error induced by neglected terms

The first type of error is the effect on modeled regenerator heat flux of estimated errors in mass flux g. Both g and its error estimate come from numerical simulation — g being the mid-sample value and its error being the variation in g

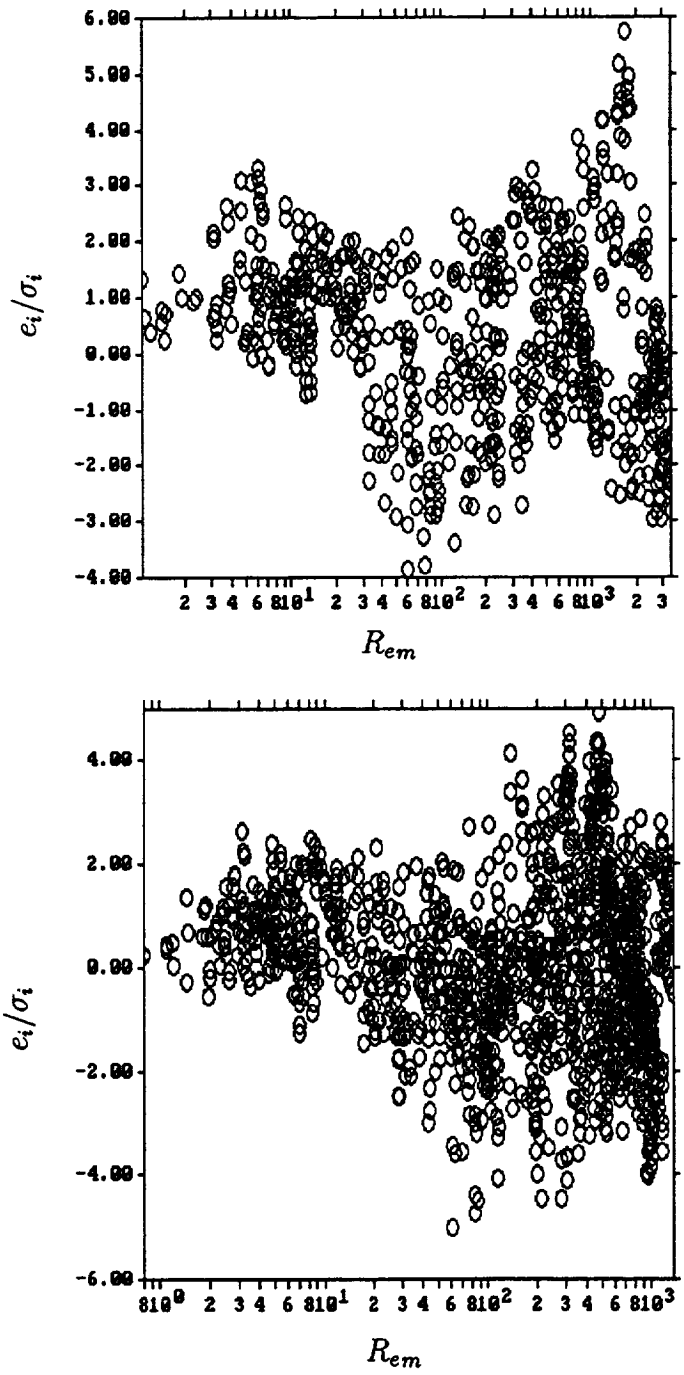

Figure 3.3: Residuals for simultaneous N_u, N_k parameter estimates: combined woven screens χ^2 = 1.86E3 with 693 points (top), combined metal felts χ^2 = 3.69E3 with 1339 points (bottom).

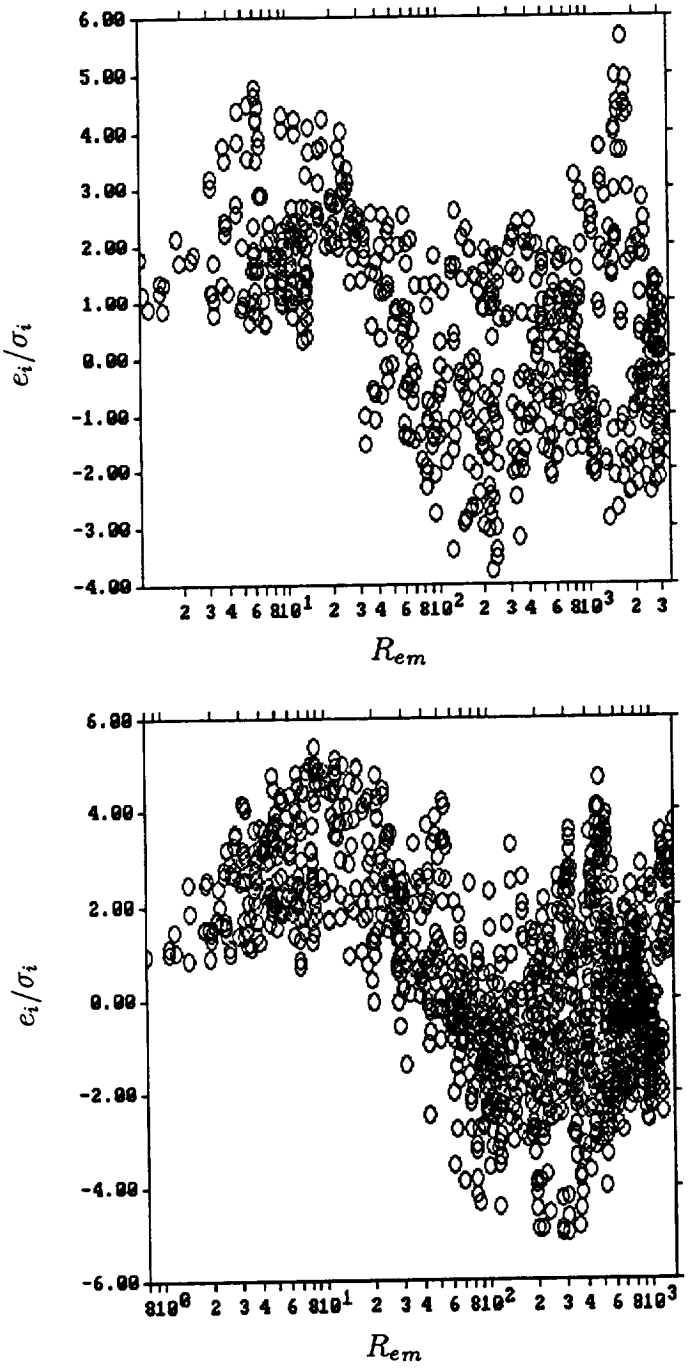

Figure 3.4: Residuals for effective N_{ue} parameter estimates: combined woven screens $\chi^2 = 2.43E3$ with 693 points (top), combined metal felts $\chi^2 = 5.97E3$ with 1339 points (bottom)

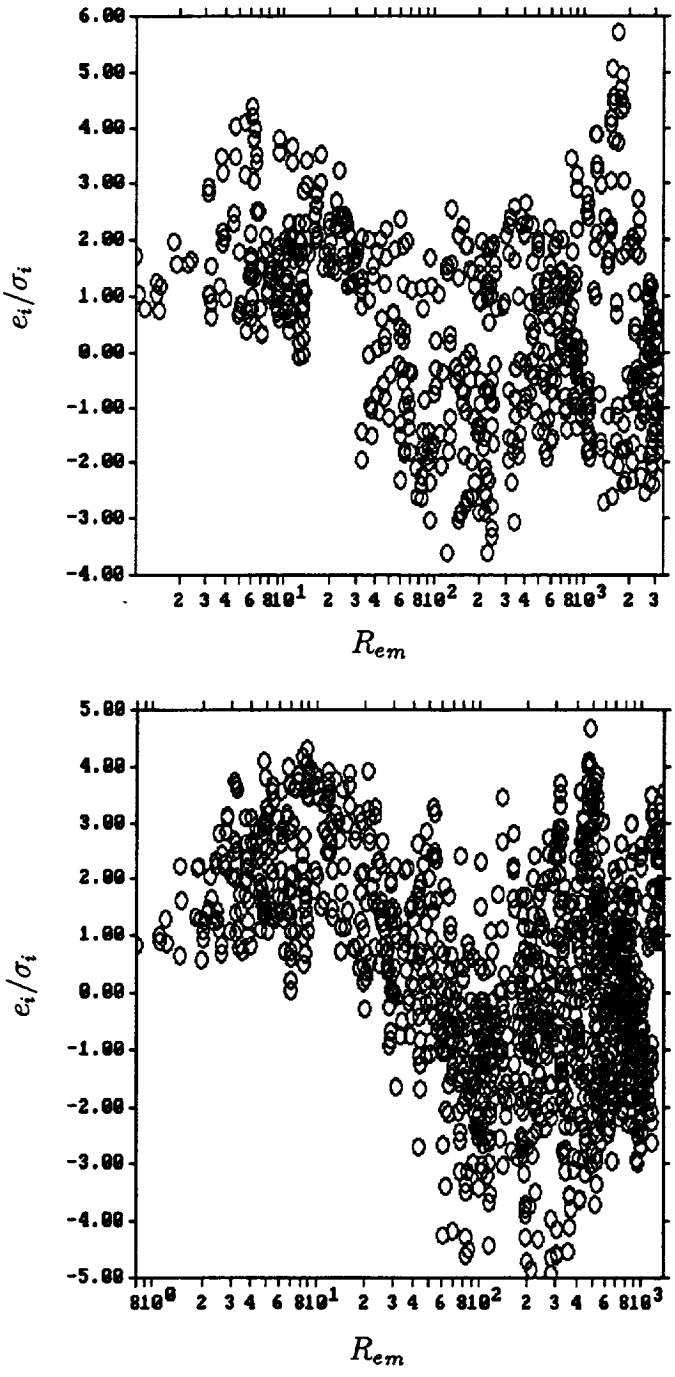

Figure 3.5: Residuals for overall heat flux N_q parameter estimates: combined woven screens χ^2 = 2.14E3 with 693 points (top), combined metal felts χ^2 = 4.79E3 with 1339 points (bottom).

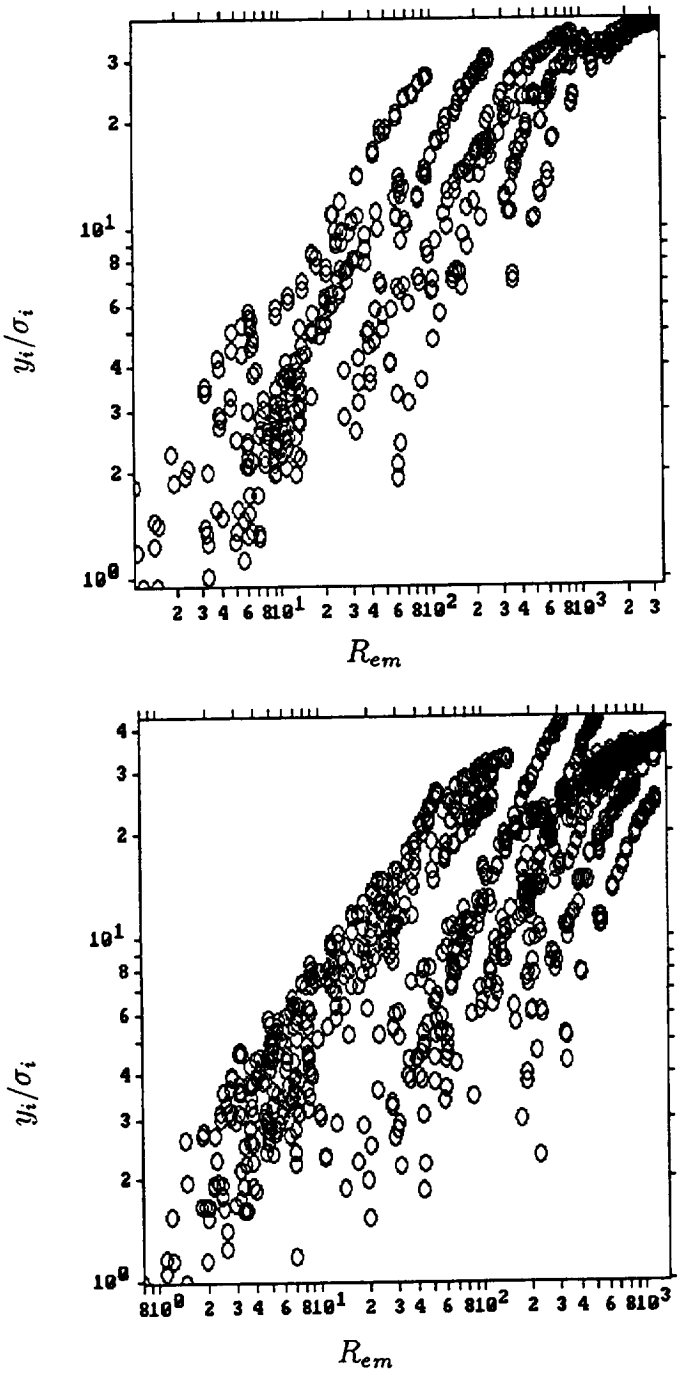

Figure 3.6: Signal to estimated-noise ratios for heat-transfer data sets: combined woven screens (top), combined metal felts (bottom).

across the sample. The second type of error is the effect on modeled regenerator heat flux of estimated errors in the presumed-constant sample midpoint temperature gradient $\frac{\partial T}{\partial x}$. All models predict linear variation of regenerator heat flux with $\frac{\partial T}{\partial x}$. The error estimate for $\frac{\partial T}{\partial x}$ is based on instrumentation error and local temperature variations related to solid-to-gas heat capacity ratio and flow tidal amplitude. The third type of error is the effect on modeled regenerator heat flux of key neglected terms in the model such as: the component of solid temperature variation that contributes to net enthalpy flux, time-varying pressure, spatially-varying mass flux and spatially-varying axial conduction. These errors only pertain to models correlating N_u, N_k or N_{ue}, not to those correlating overall heat flux N_q. Errors from all these sources were uniformly small (combined together no more than 20% of the estimated measurement error) so they have no significant effect on the results and are not shown.

3.2.3 Comparison to Other Data

Good published data for heat-transfer properties in porous materials is scarce. Our only comparison is again to the data of Kays and London [7] for woven-screen matrices, figure 7-8, p. 148. In the low Reynolds number range (for true woven-screen matrices) their correlations were based on the transient-flow technique which tracks a step temperature change in the fluid (introduced upstream of the matrix) as it emerges downstream under steady flow conditions. Data reduction correlates the heat-transfer coefficient with the maximum slope of the exit temperature-time plot, neglecting axial thermal diffusion. We are willing to ignore the differences between steady and oscillating flow because of the low Valensi numbers of our tests. But ignoring axial thermal diffusion is another thing. The presence of thermal diffusion tends to reduce the maximum slope of the exit temperature profile. Therefore, the maximum-slope method tends to underpredict heat transfer coefficient when the temperature slope is steepest — or, as our results suggest, for Reynolds numbers below about 10.

We have two candidates for comparison to the Kays and London data, our best-guess value for the true Nusselt number N_u and the effective Nusselt number assuming zero axial thermal diffusion N_{ue}. We shall compare both. Since, the assumptions behind the Kays and London correlations are consistent with our method of reducing N_{ue}, it would seem that N_{ue} offers the most meaningful comparison. However, both our N_{ue} and Kays and Londons data are likely to suffer from error at low Reynolds (Peclet) numbers, and the errors may not be the same.

In making the comparison, we should also note that Kays and London correlate heat transfer in terms of Stanton number, which is related to our Nusselt number by

$$S_t = \frac{N_u}{R_e P_r} \tag{3.1}$$

The following tables assume $P_r = 0.7$ in converting Stanton to Nusselt number and Reynolds to Peclet number.

Screen Nusselt Number Comparison – $\beta = 0.602$

R_e	4	10	40	100	400	1000	4000
N_u — Kays & London	1.04	1.81	4.16	7.10	16.1	28.1	65.6
N_u — present report	1.19	1.85	4.00	7.00	16.9	30.5	75.6
N_{ue} — present report	0.95	1.45	3.25	5.90	15.3	29.3	78.7

Screen Nusselt Number Comparison – $\beta = 0.832$

R_e	40	100	400	1000	4000
N_u — Kays & London	9.72	14.5	28.4	46.9	101
N_u — present report	7.14	12.5	30.1	54.5	135
N_{ue} — present report	5.79	10.5	27.3	52.2	140

The tables covers a Reynolds number range from 4 to 4000, which was the range of overlap for our respective data sets. Peak Reynolds number for our experiments ranged from 1.0 to 3400, while Kays and London steady Reynolds numbers ranged from about 4 (for $\beta = 0.602$) to 10^5 (for $\beta = 0.832$). Although above 1000, as mentioned above, the Kays and London data was probably for crossed-rod matrices. We expect good agreement among all three Nusselt numbers for high Reynolds numbers, and this is somewhat borne out by the tables. Best agreement is for Reynolds number about 500 with increasing disagreement at 4000, possibly because it falls just outside the top range of our data or possibly because the heat-transfer characteristics of crossed rods are a bit different than woven screens. At low Reynolds numbers where we expect the worst agreement we see that both N_{ue} and the Kays and London value are smaller than our *true* N_u, but not by much. In fact there is remarkably good agreement down there, all three predicting a suspiciously low Nusselt number. This is not surprising in light of the likelihood that enhanced axial conduction is interfering with proper Nusselt number reduction for all three at low Reynolds numbers.

Chapter 4

Concluding Remarks

The achievements of this effort have been both practical and theoretical. On the practical side we have produced correlating expressions for pressure drop and heat transfer for the two types of regenerator material commonly used in stirling engines and coolers: woven screens and metal felts. While steady-flow data for woven screens has been previously reported in [7], we have confirmed its validity for stirling use and extended its range to the low Reynolds numbers commonly found in stirling regenerators. Data for felts is new. In a break with tradition, we have placed enhanced gas conductivity on an equal footing with film heat transfer and successfully correlated expressions for both simultaneously. And we have introduced the concept of overall heat flux ratio, correlated in terms of peak Peclet number (peak $R_e P_r$), which fits the data remarkably well.

Accuracy for our derived correlations was limited by inter-sample variations not correlated with porosity (in the case of friction factor) and thermal noise at low Reynolds numbers (in the case of heat-transfer correlations). For friction factors, relative accuracy was a fairly uniform worst-case of 10% for screens and 27% for felts, over the entire Reynolds number range. This should be understood as the worst likely relative error in cycle-average pumping dissipation that would be produced by our correlations for a typical sample matrix. For heat transfer correlations the relative accuracy was more dependent on Reynolds number, principally because the measured signal was always low at low Reynolds number. Thus the worst likely relative error in cycle-average total axial heat transport ranged from about 10% at peak Reynolds number on the order of 1000 to about 50% for peak Reynolds numbers below about 5. It would be prudent then to avoid placing too much faith in our heat-transfer correlations for a situation where peak Reynolds number was much below 5. Fortunately, it is the author's observation that most stirling-cycle regenerators operate in a range significantly above this. This is corroborated by Seume and Simon ([12], fig. 7, p. 537) who found no peak Reynolds number below about 30 in a survey of about a dozen stirling engine regenerators in use at the time.

On the theoretical side we have managed to dispel some of the myths surrounding oscillating flow. Under the range of conditions we tested, which were

intended to be representative of most stirling applications, we found no essential differences compared to steady flow. (The 1992 report [4] addresses this issue in more detail.) In other words, instantaneous local Reynolds number or Peclet number ($R_e P_r$) appear to characterize the flow quite adequately. This means, for example, that porous-material friction factors obtained by others under steady-flow conditions should suffice for oscillating-flow conditions in stirling regenerators. The exception to this might be for Valensi numbers above about 20, the upper range of the values we encountered.

It is not quite so simple with heat transfer. While we agree, in principle, that heat-transfer and enhanced axial conduction also depend only on local instantaneous Reynolds number, the trick is in reducing the data — how one converts experimental measurables to Nusselt numbers, etc. There is no experimental apparatus we know of that directly measures the heat transfer coefficient in realistic regenerator matrices. The wires and void spaces are simply too small to introduce temperature transducers. So there is always some intermediate model in terms of which heat-transfer coefficient is deduced. In our case the model is a bit complicated as it involves total axial energy transport under oscillating flow conditions. Other approaches tend to track exit temperature profiles, usually under steady flow conditions. Both tend to neglect phenomena that complicate the analysis. The question is: which method is most likely to produce the correct result in a stirling engine or cooler simulation? We would argue that our method does, because it is most likely to reproduce the quantity that really matters: total energy transport down the regenerator.

Appendix A

Symbols

The following symbols are those appropriate for a computational model of porous regenerator flow where the computational grid is large compared to the matrix pore size. Accordingly, thermodynamic variables like T, u, etc., are understood in a local-average sense — spatially averaged over a large enough volume to remove eddy fluctuations, yet still small compared to the overall problem dimensions. This viewpoint is consistent with the measurement resolution in the test rig itself.

c_p	gas specific heat at constant pressure
d_h	hydraulic diameter: $d_h = 4/s$
e_i	error of ith data point; difference between measured y_i and theoretical value
g	mass flow rate per unit void area: ρu
g_m	peak value of g
h	heat transfer coefficient between gas and solid matrix
h_e	effective heat transfer coefficient that includes the effects of k_a when used in an oscillating-flow regenerator model
k	molecular gas conductivity
k_a	apparent agitated-flow gas axial conductivity (based on mean void flow area)
L	test-sample length
P	pressure
q_h	part of q_t attributed to enthalpy transport (finite h)
q_k	part of q_t attributed to apparent axial conduction
q_t	time-average total energy flux (per unit void area) down the regenerator
q_t^*	q_t, less static conduction
s	matrix surface area per unit void volume
t	time
T	gas temperature (local void average)
T_s	solid matrix temperature (local solid average)
u	gas velocity (local void average)
x	axial coordinate
y_i	measured value of ith data point
β	porosity (void volume / total volume)
μ	molecular gas viscosity (local void average)
ρ	gas density (local void average)
σ_i	advanced estimate of e_i based on random measurement error
ω	angular frequency (rad/s)

Dimensionless Groupings

f	Darcy friction factor: $d_h \frac{\partial P}{\partial x} / (\rho \frac{u\|u\|}{2})$
N_k	axial conductivity enhancement ratio: $\frac{k_a}{k}$
N_{k0}	value of N_k at static flow conditions
N_u	Nusselt number: $\frac{h d_h}{k}$
N_{ue}	effective Nusselt number: $\frac{h_e d_h}{k}$
N_q	overall heat flux ratio: $q_t^* / (k \frac{\partial T}{\partial x})$
P_e	Peclet number: $R_e P_r$
P_{em}	peak Peclet number: $R_{em} P_r$
P_r	Prandtl number: $\frac{\mu c_p}{k}$
R_e	Reynolds number: $\frac{g d_h}{\mu}$
R_{em}	peak Reynolds number: $\frac{g_m d_h}{\mu}$
V_a	Valensi number: $\frac{\rho \omega d_h^2}{4\mu}$
δ / L	tidal amplitude ratio: $g_m/(\rho \omega L) = (d_h/(4L)) R_{em}/V_a$
β	porosity: void volume / total volume

Subscripts

0	static-flow value
m	peak value (amplitude of first harmonic)

Operators

$\langle\rangle$	time average over one cycle: $\langle f \rangle = \frac{\omega}{2\pi} \int_0^{2\pi/\omega} f dt$

Appendix B

Hardware

In its heat-transfer mode, the test rig measures exactly the quantity that is of bottom-line importance in stirling machines: net thermal energy flux. And it does this over a wide range of operating conditions typical of stirling designs.

The essential idea is to attach, in sequential fashion, a cooler, regenerator sample and heater to a piston cylinder. The assembly is oriented so the heater outlet opens into a relatively large fixed volume. When the rig is motored, an oscillating gas flow is set up in the regenerator sample. Moreover, due to the large volume of the system, the pressure swing in the piston cylinder is due predominantly to the frictional pressure drop of the regenerator sample and heat exchangers and not to compression effects. Therefore, the gas mass flow rate is very nearly sinusoidal and spatially uniform in all three heat exchangers.

The rig is motored with the heater temperature elevated about 200 C above the cooler temperature causing a temperature gradient to develop in the regenerator. As a consequence of axial conduction and imperfect heat transfer, a net thermal flux occurs across the regenerator, and is ultimately rejected in the cooler, where it is measured. Piston PV power (due to the pressure drop across the system) and static conduction losses through cylinder walls and flanges also contribute to cooler heat rejection, but these may be calibrated out. By doing so, the thermal performance of the regenerator in isolation can be inferred.

Refinements of these essential ideas are necessary to reduce the above conceptual scheme to practice. Some key refinements are listed below.

- The volume into which the heater gas flows is thermally insulated from its cold surroundings to prevent the influx of cold gas during the suction stroke from placing a large thermal load on the heater.
- To minimize the effects of non-regenerator thermal losses, the regenerator sample canister is fabricated out of insulating material. Moreover, the cooler is also insulated from its surroundings to prevent heat from unwanted sources being rejected in the coolant. The heater exterior is also insulated to prevent undue heating of the gas within the pressure vessel.

- Jet penetration from the heat exchangers into the faces of the regenerator might pose a problem in some samples. To avoid this as much as possible, flow diffusers are incorporated between the heat exchangers and the test sample.

For purposes of pressure drop testing the rig is somewhat simplified. The cooler, heater, and flow diffusers are removed and the sample canister attached directly to the piston cylinder.

B.1 Early History

The current test rig is actually a modified form of an earlier pressure-drop test rig designed by Sunpower Inc. for NASA-Lewis. Reference [8] describes this rig in detail and figure B.1 shows it in cross section. Several components of the earlier rig remain the same. At the heart of the rig is a variable stroke and variable frequency linear drive motor. A displacement section, consisting of a single close fitting piston in a cylinder, is directly attached to this linear drive motor. The test section is connected to the other end of the displacement section. The assembled motor, displacement, and test section are then enclosed in an outer pressure vessel to allow for operation at elevated mean pressures.

The versatility of the basic test rig is shown by the wide range of operating parameters listed in the following table:

Rig Operating Parameters

stroke (cm)	0 – 3.0	
frequency (Hz)	<1 – 120	
mean pressure (bar)	0 – 151	(absolute)
motor power (kW)	0 – 2	(at 60 Hz, 3 cm stroke)
piston diameter (cm)	1.9	(standard configuration, larger and smaller pistons possible)

For regenerator heat transfer testing, the test section of the original pressure drop rig (a single element) was replaced by a multiple element unit consisting of a cooler, regenerator, heater and buffer volume. The design and fabrication of this setup was performed by Sunpower Inc. for NASA-Lewis under contract NAS3-25620. A detailed description of this hardware is given in reference [3].

B.2 Current Rig Description

The rig was again modified during testing at the Ohio University Center for Stirling Technology Research (CSTR). Figure B.2 shows a cross sectional drawing of the test section of the rig as presently configured for heat-transfer testing. Pictures of the test rig are presented in figures B.3, B.4 and B.5.

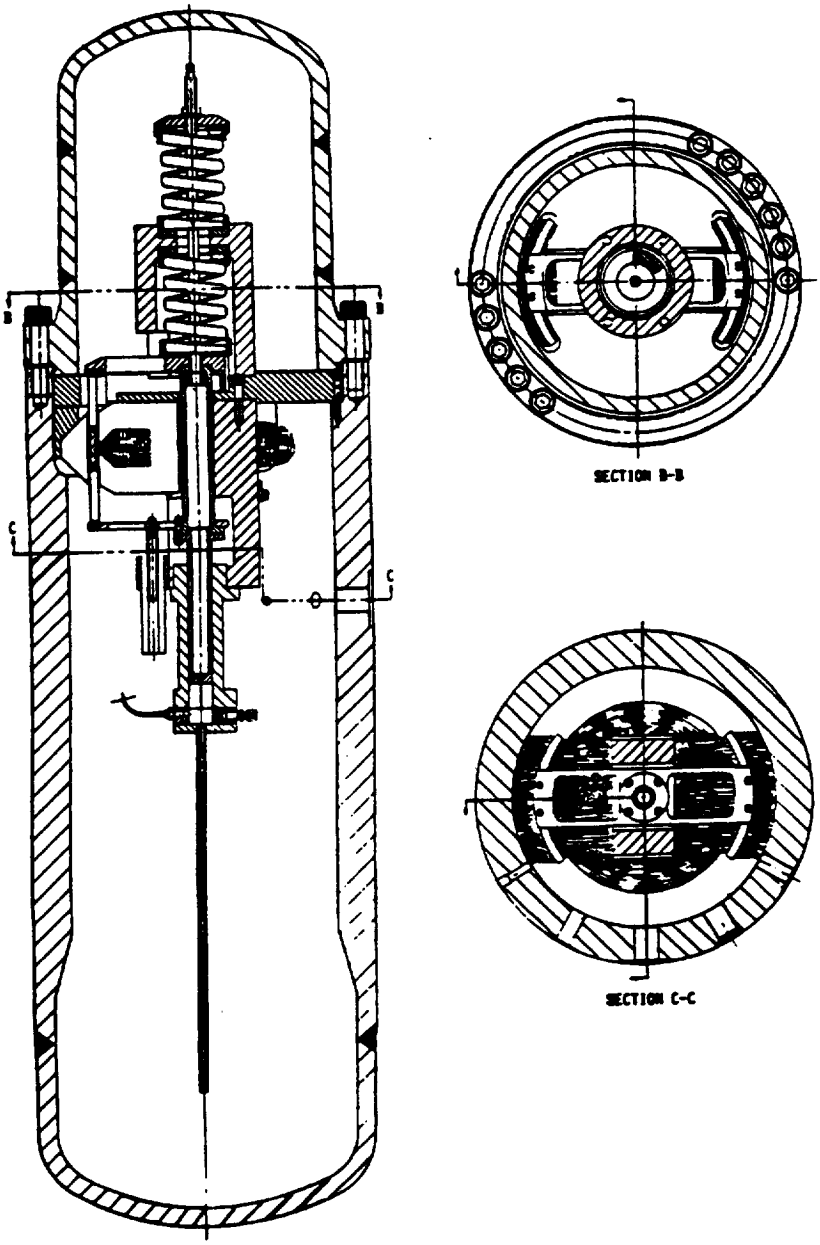

Figure B.1: Cross sections of original pressure drop test rig prior to modification into the current heat-transfer-capable test rig.

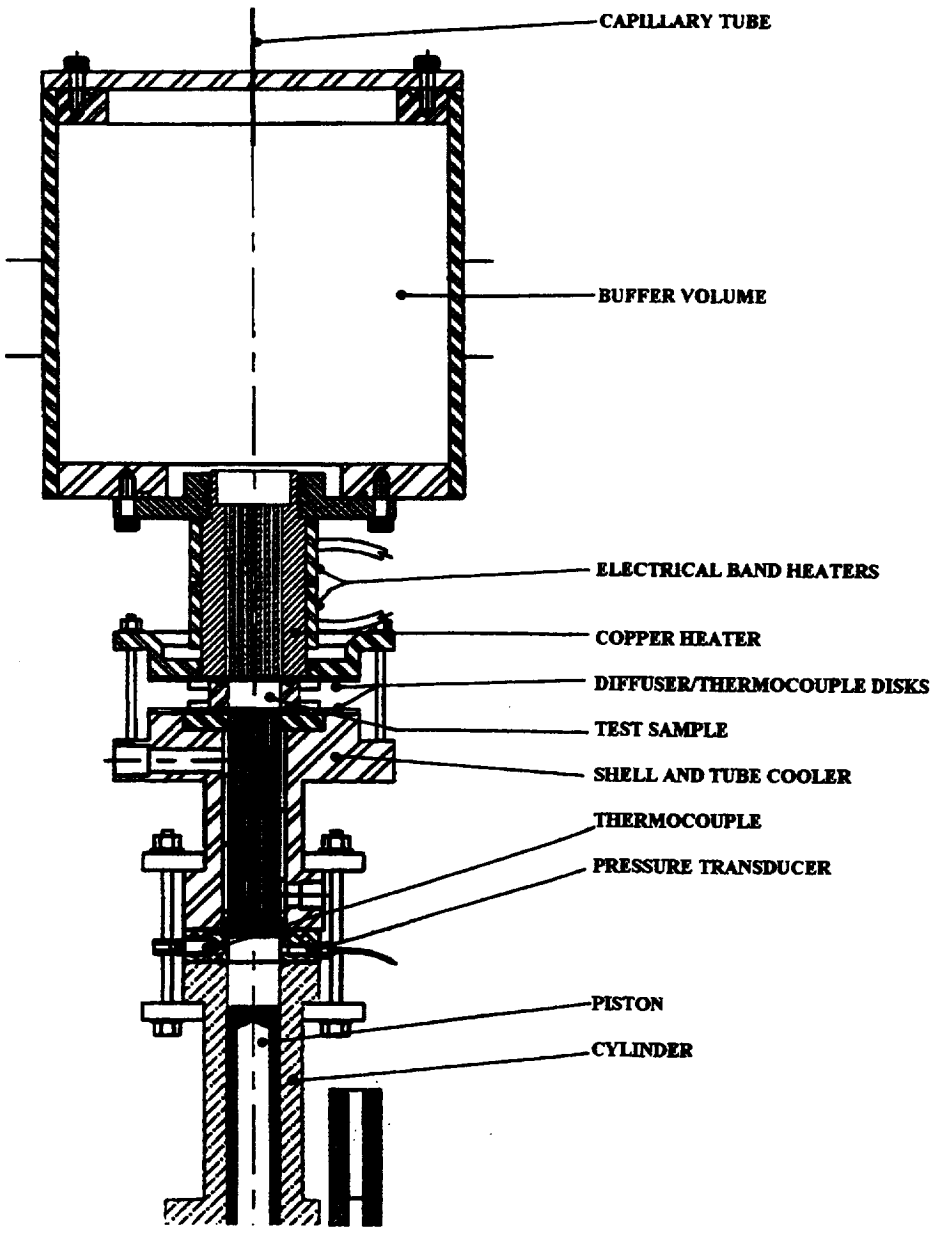

Figure B.2: Cross section of current regenerator test rig in heat-transfer testing mode.

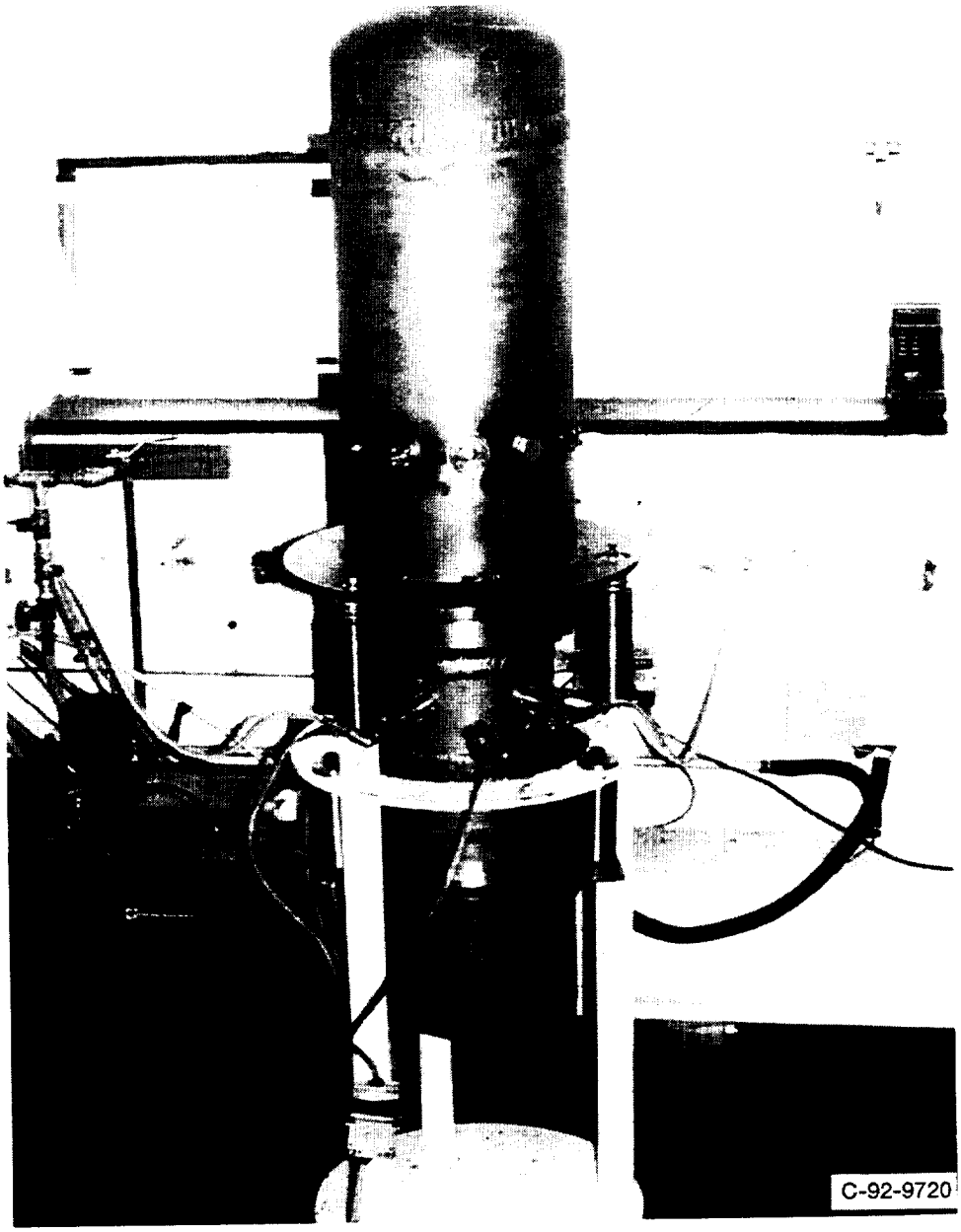

Figure B.3: Assembled Regenerator Test Rig.

Figure B.4: Regenerator test rig internal assembly with insulation installed. Scale shown by co-author Gary Wood

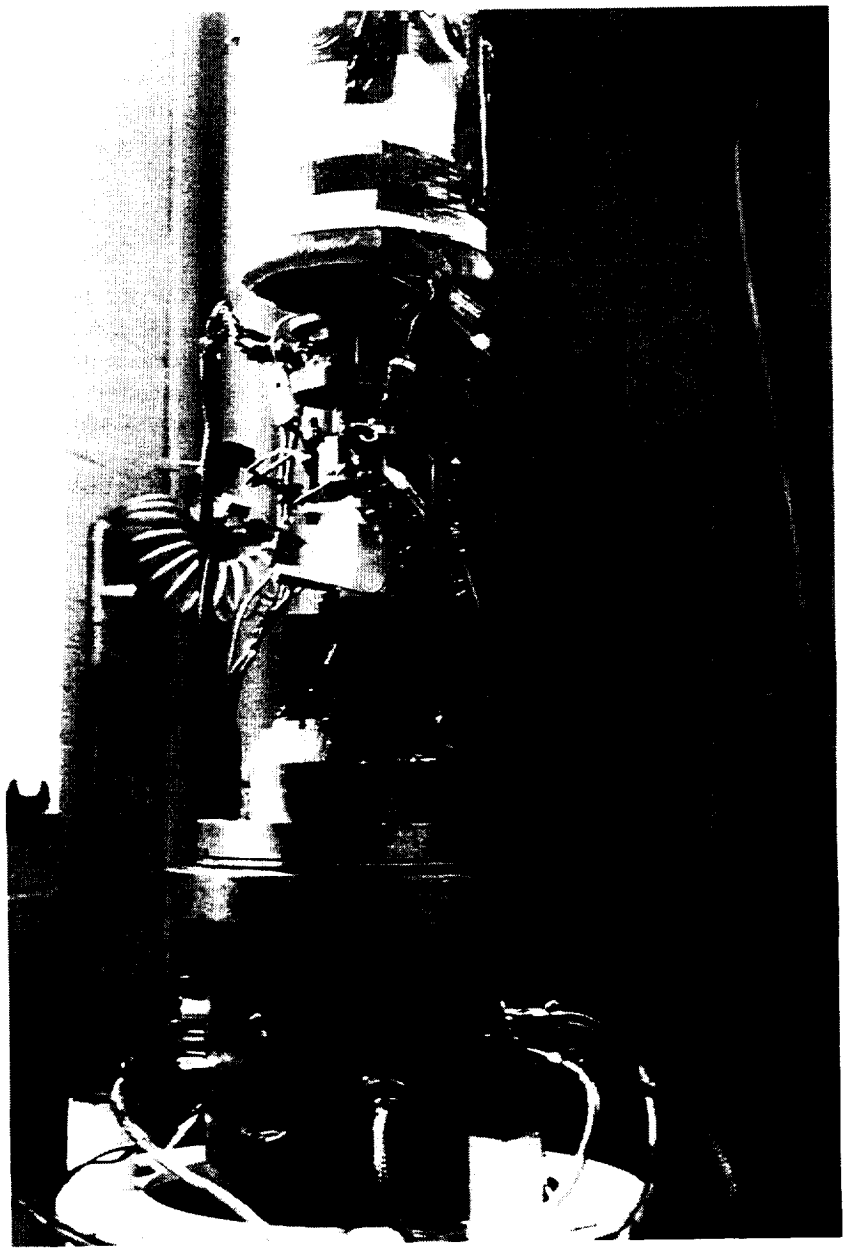

Figure B.5: Regenerator test rig internal assembly detail, without insulation.

B.2.1 Rig Orientation

The rig had been originally designed for operation with the hot end down. Early testing at CSTR indicated that significant convection losses were occurring in spite of the installed insulation. So, the rig was inverted to reduce these convection losses. This also allowed the test rig to come to steady state more quickly, especially when the pressure level in the rig was changed.

B.2.2 Buffer Volume

The buffer volume, attached to the end of the heater opposite the end connected to the test section, is a thermally-insulated canister for the purpose of containing the hot gas exiting the heater. An inadvertent side-effect was that it prevented timely pressure charging or discharging because the only gas pathway from the buffer volume to the pressure vessel interior was the piston clearance seal, which was very effective.

So, we added the capillary tube seen in the drawing to vent the buffer volume to the interior of the outer pressure vessel, sized so as to give reasonable charging times, while not affecting the accuracy of the measurements.

B.2.3 Heater Section

The heater section was originally a shell and tube heat exchanger. Heat was supplied by means of a pumped (closed) Dowtherm loop. The heating element and the pump were external to the outer pressure vessel of the test rig, with the fluid carrying lines passing into the vessel through the pressure vessel extension.

To simplify this system we replaced it with a copper cylinder having drilled flow passages. Heating is supplied by means of two electrical band heaters clamped to the outside of this cylinder. Heat input is controlled by a commercial temperature controller.

B.2.4 Sample Holder and Diffuser/Thermocouple Disks

As originally designed the test samples had Viton rubber molded around them. Five fine-wire thermocouples were then installed on each face of the regenerator. Finally diffuser disks were glued onto both faces, outside the thermocouples.

This process of vulcanizing Viton around the sample was tried at CSTR, but was found to be difficult to predict and control. The process variables (molding heat and pressure) had to be modified for each sample.

Because of this and other problems we devised an alternative process. We decided to place the samples in Torlon holders. Torlon (an Amoco Corp. trade-name for polyamide-imide) was selected because of its good temperature and insulating properties, as well as the availability of a particular grade having expansion characteristics almost identical to material of the samples themselves. Two separate methods were devised here, one each for the two different types of samples which we planned to test.

In the case of a sintered rigid material, Torlon holders were heat shrunk around the sample. Samples were cooled with liquid nitrogen and the Torlon heated in an oven before assembly.

For stacked screen samples, the screens were first aligned and clamped between centers in a lathe. The outside surface of this stack was then coated with a high temperature (260 C, 500 F) epoxy, and allowed to cure. Once cured, the outside surface of epoxy was machined round. Then several screens were peeled off each face of the sample to determine the level of penetration of the epoxy. Here instead of a heat shrink process the Torlon holders were fabricated with inside diameter O-rings for sealing against the outside of the sample.

To provide for the thermocouples and the diffuser disks we fabricated reusable holders, separate from the test sample. These were fabricated from G7 phenolic. Sealing on the face of these next to the heat exchangers was accomplished by means of silicone glue. On the faces adjacent to the test sample, sealing was provided by O-rings with the grooves cut into the face of the Torlon holders. A picture of a diffuser/thermocouple disk and two test samples in their Torlon holders is shown in figure B.6.

B.2.5 Cooler

The cooler is a shell and tube heat exchanger using water as the coolant. Originally type K thermocouples had been selected for measuring the temperature rise of the coolant. To improve the measurement of heat rejection we replaced these with high accuracy (0.1 C interchangeable) thermistor probes from Omega. Here we obtained several probes (for spares) and selected the two best matched thermistors from the group.

To further improve the measurement of heat rejection we replaced the original coolant flow sensor with an Omega model FTB601 having much less pressure drop and a lower flow range (linear range 0.1- 2.0 LPM). This flow sensor allowed us to reduce coolant mass flow significantly and also allowed us to install a constant head flow system.

To solve the problem of inlet coolant (tap water) temperature changes over time, we installed a laboratory cooling bath. Cooling water passed through the bath in coiled copper tubing, before proceeding to the test rig.

B.3 Data Acquisition

The DAS (Data Acquisition System) of the original Pressure Drop Test Rig consisted of a Metrabyte analog-to-digital board installed in an IBM compatible computer.

For regenerator testing, we added a submultiplexer board to handle the numerous additional non-dynamic signals (mostly thermocouples). Here we chose (because of cost) a board advertised as equivalent to a Metrabyte submultiplexer, but made by a different manufacturer.

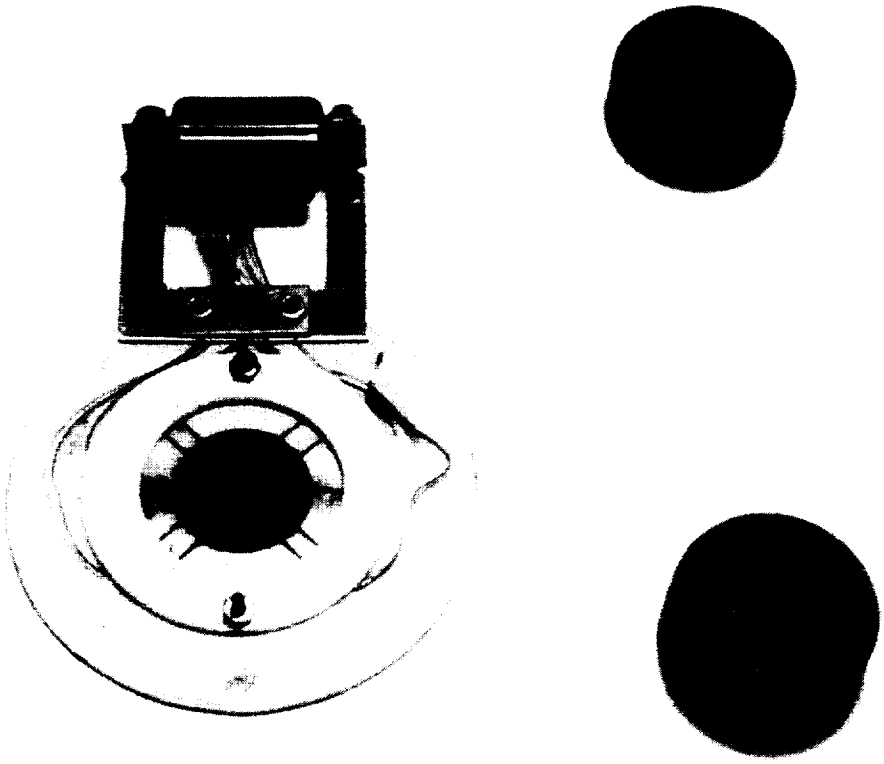

Figure B.6: Diffuser/thermocouple disk and test samples in Torlon holders.

After much trouble-shooting we tracked erroneous temperature readings to a poorly sized resistor in the open thermocouple detect circuits on this board. The company acknowledged our finding and sent us replacement resistors. Because of time constraints, we did not install these resistors but decided to simply disable the *detect* circuits.

B.4 Test Procedures

Pressure-drop testing is relatively straight forward. With only the regenerator test sample bolted to the end of the piston cylinder, the rig is charged to pressure and the motor is swept over a range of strokes and frequencies, during which a number of data points are logged. The important measured quantities are piston displacement and cylinder pressure as functions of time. These are integrated together to give PV power dissipation, which is the actual basis for friction-factor data reduction. During testing, the operator keeps an eye on the piston displacement and pressure traces as displayed on an oscilloscope to make sure that meaningful data is being logged, which he does by pressing the appropriate key at the computer console. The process is repeated with at least two working gases (helium and nitrogen) to ferret out any gas-property dependence in testing or data reduction where none should be.

Heat-transfer testing is substantially similar. This time, however, the complete assembly shown in figure B.2 is in place, the heater temperature raised and heat rejection to the cooler is added to the important measured quantities. The elevated heater temperature poses a tactical difficulty because of time required to establish equilibrium temperatures in the entire apparatus. Because of this, the rig is generally heated and operated for several hours before logging data. A change in charge pressure or gas requires additional equilibrating time. And during testing the thermal boundary conditions tend to change with changing piston stroke and frequency. This requires the operator to log several zero-amplitude points over the course of a run so that the background component of heat rejection to the cooler (steady conduction through walls, flanges, insulation and the matrix itself) can be calibrated out of the data.

Appendix C

Experimental Models

C.1 Heat-Transfer Model

The two main mechanisms for axial energy transport in regenerators are enthalpy transport and axial conduction. Therefore, the net cyclic regenerator energy flux per unit void area may be expressed as

$$q_t = q_h + q_k \tag{C.1}$$

where q_h is enthalpy transport per unit void area given by

$$q_h = \langle c_p g T \rangle \tag{C.2}$$

and q_k is apparent axial conduction per unit void area given by

$$q_k = -\frac{\partial T}{\partial x} \langle k_a \rangle \tag{C.3}$$

The operator $\langle\,\rangle$ indicates time average and k_a is the apparent axial conduction coefficient (a function of flow variables) comprising molecular conduction, matrix solid conduction and thermal diffusion arising from small-scale flow eddies. The above form for q_k is valid since all three effects depend linearly on temperature gradient. We assume $\frac{\partial T}{\partial x}$ is roughly constant, and gas and solid temperatures are nearly identical so that $\frac{\partial T}{\partial x}$ is representative of the solid temperature gradient as well.

The above expression for q_h is not yet useful to us because it does not explicitly contain the film heat transfer coefficient h for which we are trying to solve. However, it is straightforward to make the dependence of q_h on h explicit. Substituting the identity $T = (T - T_s) + T_s$ into equation (C.2) gives

$$q_h = \langle c_p g (T - T_s) \rangle + \langle c_p g T_s \rangle \tag{C.4}$$

Now, the second time average on the right is negligible for two reasons: (1) the variation in T_s is small and (2) it is 90 degrees out of phase with g — at least for

sinusoidal flow. Furthermore, $T - T_s$ in the first time average may be replaced using the approximate equation

$$T_s - T = \left(\frac{c_p g}{hs}\right) \frac{\partial T}{\partial x} \tag{C.5}$$

leaving the following expression for q_h

$$q_h = -\frac{{c_p}^2}{s} \frac{\partial T}{\partial x} \left\langle \frac{g^2}{h} \right\rangle \tag{C.6}$$

now, explicitly containing h.

Equation (C.5) comes from a simplified form of the one-dimensional gas energy equation for the porous matrix. The starting point is the complete equation in the form

$$\frac{\partial}{\partial t}(\rho e) + \frac{\partial}{\partial x}\left((\rho e + P)u + q\right) - Q = 0 \tag{C.7}$$

Matrix-to-gas heat transfer per unit void volume Q can be expressed in terms of a film heat transfer coefficient h as

$$Q = hs(T_s - T) \tag{C.8}$$

Ignoring the $u^2/2$ term in e and expressing $\rho e = (c_v/R)P$ and $\rho e + P = c_p \rho T$ gives the alternate form of the energy equation

$$(c_v/R)\frac{\partial P}{\partial t} + \frac{\partial}{\partial x}\left(c_p g T + q\right) + hs(T - T_s) = 0 \tag{C.9}$$

At this point, some further assumptions simplify the energy equation:

1. $\frac{\partial P}{\partial t}$ is negligible.
2. g is uniform in x (although it varies with time).
3. The matrix temperature profile is linear, with constant $\frac{\partial T}{\partial x}$.
4. Apparent conductivity k_a is not a function of x.

Assumption 1 means that the first term in (C.9) is negligible. This is valid since there is no significant pressure swing in the proposed rig. Assumption 2 allows us to factor g from the second term of (C.9). This is valid to the extent that assumption 1 holds and temperature at any location in the matrix does not fluctuate too much. Assumptions 3 and 4 allow us to neglect $\frac{\partial q}{\partial x}$ for then $\frac{\partial q}{\partial x} = k_a \frac{\partial^2 T}{\partial x^2} \approx 0$.

With the above assumptions, the gas energy equation for the porous matrix becomes

$$c_p g \frac{\partial T}{\partial x} = hs(T_s - T) \tag{C.10}$$

which is easily solved to give equation (C.5) for the gas-to-matrix temperature difference.

Equations (C.3) and (C.6) form the basis for subsequent data modeling. They are valid to the extent that the approximations used in obtaining them are valid — which some readers are likely to question at this point. While it is beyond the scope of the present report, a complete discussion of error estimation can be found in the earlier report [3].

C.1.1 Dimensionless Forms

The next step is to re-write the equations for q_h and q_k in terms of dimensionless groups. Because of the simple expression for q_h that will result, we choose to represent h in terms of Nusselt number rather than Stanton number. At any rate, the two are related by $N_u = S_t R_e P_r$. Starting with equation (C.6) and rearranging in terms of Nusselt number (hd_h/k), Peclet number ($gd_h c_p/k$) and hydraulic diameter ($4/s$), gives

$$q_h = -k\frac{\partial T}{\partial x}\left\langle \frac{P_e^2}{4N_u} \right\rangle \tag{C.11}$$

To represent apparent axial conductivity, we choose the dimensionless grouping $N_k = k_a/k$, the ratio of apparent conductivity to gas-molecular conductivity. In terms of N_k, (C.3) reduces to

$$q_k = -k\frac{\partial T}{\partial x}\langle N_k \rangle \tag{C.12}$$

That N_u and N_k are good choices for dimensionless groups, is born out by the simplicity of the resulting expressions for q_h and q_k and the common factor $k\frac{\partial T}{\partial x}$ occurring in both.

In our test rig it is the enhancement of axial conduction above molecular conduction we are correlating, or $q_k - q_{k0}$. It is not our purpose to measure q_{k0}. In fact, we have essentially ignored it by calibrating it out of the data acquisition process. What we have measured is the total regenerator energy flux less static conduction — what we call q_t^* — defined as

$$q_t^* = q_h + q_k - q_{k0} \tag{C.13}$$

This is because there is no good way to separate q_{k0} from the other static conduction leaks that must be calibrated out of the test rig. Since, our method of measuring regenerator energy flux is not direct but, rather, based on inference from cooler heat flux, piston PV power, and various thermal conduction leaks through canister and flanges, using q_t^* as the fundamental experimental variable just means we lump q_{k0} in with the other static conduction leaks.

Equations (C.11) and (C.12) enable us to solve for N_u and N_k as functions of appropriate dimensionless groups of the flow (We will return to this). But what are the appropriate dimensionless groups? Dimensional analysis for heat transfer problems, in steady and oscillating flow, have led past researchers to the following possibilities:

- Reynolds number R_e
- Prandtl number P_r
- Valensi number V_a
- Length to diameter ratio L/d_h
- Mach number
- Grashof number

For regenerator flow we categorically reject the Mach and Grashof numbers. Mach number is only important when flow velocities approach sonic velocity — our flow velocities should never exceed the order of 10 m/s. Grashof number is only important when buoyancy forces are significant.

More tentatively, we reject L/d_h and Valensi number. L/d_h measures the ratio of the total matrix flow length to the depth into the matrix required to establish velocity and temperature fields. Normally, L/d_h is sufficiently large that we can ignore entrance effects. Valensi number is proportional to the square of the ratio of hydraulic diameter to viscous boundary layer thickness in oscillating flow. It measures the tendency of fluid velocity near the middle of flow channels to lag behind that near the walls in response to oscillating pressure gradients. In laminar channel flow, this phenomenon does not seriously affect heat transfer until V_a approaches about 100. Normally, V_a is no more than the order of 10 for most regenerators.

This leaves only Reynolds number and Prandtl number as potential correlating groups. The question is: R_e, P_r separately, or together as Peclet number $P_e = R_e P_r$? Roughly speaking, R_e is inversely related to the thickness of the viscous boundary layer while P_r is proportional to the ratio of the viscous to thermal boundary layer thickness. It is somewhat intuitive, then, to expect film heat transfer to correlate with the product of R_e and P_r. Schlichting ([11], pp. 298), for example, concludes that for laminar flow over a flat plate

$$N_u \propto \begin{cases} \sqrt{P_r}\sqrt{R_e} & \text{for } P_r \to 0 \\ \sqrt[3]{P_r}\sqrt{R_e} & \text{for } P_r > 0.6 \end{cases} \tag{C.14}$$

The question of correlating in terms of P_r is somewhat moot anyway, since past evidence suggests that all experiments will be done with gases where $P_r \approx 0.7$. At least, if we chose P_e to represent our data, then there is some hope that our correlations will apply to non $P_r = 0.7$ cases (liquid metals, etc.).

So we are led to chose correlations for N_u and N_k in terms of Peclet number alone, as in correlations (2.6) and (2.7). Of course when extended over a range of similar matrix structures, we introduce other relevant dimensionless characterizations such as porosity.

C.1.2 Separating q_h and q_k

So how is it that equations (C.11) and (C.12) enable us to solve for N_u and N_k independently when we are measuring q_h and q_k combined together in total regenerator energy flux? The completely honest answer is they cannot. If we are allowed no further assumptions about q_h and q_k then there is no way they can be separated from q_t^*. But if we assume only that both N_u and N_k scale as Peclet number raised to some exponent, and that the exponent is less than one and about the same for both, then we can separate them. These assumptions are justified by the typical success by others in correlating N_u and N_k in exponential forms and by arguments for similar scaling of N_u and N_k presented in appendix F.

The key observations are the dependence of q_h in equation (C.11) on the time-average of P_e^2/N_u and of q_k in equation (C.12) on the time average of N_k only. If N_u and N_k both scale with P_e^a, then the q_h and q_k will scale respectively with the time-average of P_e^{2-a} and P_e^a. So if $a < 1$, the q_k part of total heat flux will be relatively more significant at low P_e values and the q_h part will be more significant at high P_e values. For example, if $a = 1/2$ (not too unreasonable) then q_h will scale as $P_e^{3/2}$ while q_k will scale as $P_e^{1/2}$. It is not to hard to imagine then, that testing over a broad enough range of Peclet numbers will allow our data reduction process to accurately estimate exponent a.

C.1.3 Cycle-Averaged Form

The preceding analysis suggests an alternative method of correlating total regenerator energy flux q_t^*. Instead of correlating instantaneous N_u and N_k in terms of instantaneous Peclet number, it might be sufficient for many purposes to correlate q_t^* directly in terms of the peak Peclet value P_{em} or amplitude, presuming it varies sinusoidally over a cycle period. This is plausible because we have shown above that q_t^* may be written in the form

$$q_t^* = -k\frac{\partial T}{\partial x}\langle f(P_e)\rangle \tag{C.15}$$

where $f(P_e)$ is some function of Peclet number. If we assume that the time average of the function of Peclet number on the right scales with the peak Peclet number, then we are led to a correlation of the form (2.4), for the dimensionless group

$$N_q = \frac{q_t^*}{k\frac{\partial T}{\partial x}} \tag{C.16}$$

C.2 Pressure-Drop Model

Flow friction in the matrix produces pumping loss, which we indirectly measure in the form of piston PV power. For pressure drop tests, the sample alone is attached to the piston cylinder, without cooler, heater or flow diffusers. Letting

w_r denote the mean effective pumping power per unit void volume, it follows from the usual pumping dissipation arguments that

$$w_r = -\left\langle \frac{\partial P}{\partial x} u \right\rangle \tag{C.17}$$

where $\frac{\partial P}{\partial x}$ is the regenerator frictional pressure gradient, u is the local void-average gas velocity. Expressing the frictional pressure drop in the standard Darcy friction factor formulation gives

$$\frac{\partial P}{\partial x} = -\frac{f}{d_h} \rho \frac{u|u|}{2} \tag{C.18}$$

where d_h is hydraulic diameter and ρ is density. Substituting this equation into the previous one gives

$$w_r = \frac{1}{2d_h} \langle f \rho u^2 |u| \rangle \tag{C.19}$$

It is convenient to go one step further and rewrite this in terms of mass flux per unit area $g = \rho u$, which was one of the key variables used for the previous heat-transfer models.

$$w_r = \frac{1}{2d_h} \left\langle f \frac{g^2 |g|}{\rho^2} \right\rangle \tag{C.20}$$

We then correlate f in terms of Reynolds number, as in correlations (2.1) or (2.2).

C.3 Model Evaluation

An important part of the parameter estimation process we are about to describe, has to do with actually evaluating the right-hand sides of equations like (C.11), (C.12) and (C.20) for comparison against measured experimental values for the left-hand sides — regenerator heat flux and pumping dissipation. This is done by numerical simulation of the test rig using a finite difference algorithm based on former GLIMPS [5] computational algorithm. Each data point requires a separate simulation which is adjusted to match experimental measurables. For pressure-drop testing the friction factor in the matrix is adjusted until the piston PV power is correct. For heat-transfer testing, both matrix friction factor and heat-transfer coefficient are adjusted until PV power and cooler heat rejection are correct. The purpose of the simulation is primarily to provide mass flow rate through the sample as a function of time. The friction factor and heat-transfer coefficients in the simulation have nothing to do with the final correlations obtained by fitting the data to equations (C.11), (C.12) and (C.20).

Appendix D

Parameter Estimation

Two good references on data modeling are: Y. Bard, *Nonlinear Parameter Estimation* [1] and W.H. Press *Numerical Recipes* [10]. The first book is mostly theoretical but very complete. The second book treats data modeling as just one topic of the spectrum of numerical arts. It is concise, readable and geared toward practicality, with source code listings for all its algorithms. Our data reduction mostly followed *Numerical Recipes*' recommendations.

In its most abstract form, nonlinear data modeling begins with a model equation

$$y = f(\mathbf{x}, \mathbf{a}) \tag{D.1}$$

where y represents the dependent experimental variable $\mathbf{x}$ represents the independent experimental variables and $\mathbf{a}$ represents a set of parameters, a_k for $k = 1, \ldots, M$ which enter into the functional expression for f in a nonlinear way and are to be determined to best fit a set of data. Equation (D.1) might correspond to correlations (C.11), (C.12) or (C.20), where N_u, N_k or f are written as expressions involving unknown parameters.

Given a set of N experiments, indexed by $i = 1, \ldots, N$, one may express the measured y_i in terms of the model equation (D.1) as

$$y_i = f(\mathbf{x}_i, \mathbf{a}) + e_i \tag{D.2}$$

where the e_i are the so-called residuals — the differences between the measured and theoretical values of y. If the model is good, then the residuals are predominantly due to random and normally-distributed measurement errors. Assuming that this is the case, and assuming we can estimate in advance the standard deviations σ_i of the residuals, then the maximum likelihood estimate for the model parameters a_k is found by minimizing the least-squares objective function

$$\chi^2(\mathbf{a}) = \sum_{i=1}^{N} \left(\frac{y_i - f(\mathbf{x}_i, \mathbf{a})}{\sigma_i} \right)^2 \tag{D.3}$$

Even when the residuals are not random, equation (D.3) still makes good intuitive sense as an objective function.

The reason for the χ^2 notation goes back to probability theory. If the residuals e_i are normally distributed with standard deviation σ_i, then the minimum $\chi^2(\mathbf{a})$ (denoted χ^2_{min}) turns out to have the well-known chi-square distribution with $N - M$ degrees of freedom. This is in the sense of large numbers of experimental realizations. We use this observation to check how well our model fits the data since the probability that a chi-square distributed variable with $N-M$ degrees of freedom exceeds a certain value by chance can be easily computed. Thus, given the value χ^2_{min}, one can determine how likely it is. If it is not likely at all (probability less than 10^{-3} or so), then it must be the case that either (1) the model does not fit the data or, (2) the σ_i were underestimated. Depending on degree, alternative (1) is not necessarily bad. For a very careful experiment with low measurement error, one expects systematic model errors to dominate.

To get a more complete picture of the degree to which the model fits the data, we plot the normalized residuals e_i/σ_i vs. peak Reynolds number. Theoretically for a good data fit, this plot should be randomly distributed with standard deviation 1. Random fluctuations larger than this signify underestimated σ_i; non-random trends signify an imperfect model.

Once we have determined the maximum likelihood parameters a_k and concluded that they do indeed fit the data, we have yet another question we must ask: To what degree of accuracy have we determined the a_k. In other words: Might some other *nearby* values of the a_k fit the data nearly as well? Or, what is the sensitivity of the model to changes in the a_k parameters?

The following ideas are taken pretty much from section 14.5 of *Numerical Recipes*. Essentially we are trying to determine analytically the spread of model parameters $\mathbf{a}$ that would result from a large number of experimental realizations of our data set. We are focusing on just one component a_k at a time and want to predict its distribution in the universe of experimental realizations.

First, what is the general relationship between changes in χ^2 and changes in $\mathbf{a}$? Evidently, this depends on the functional form of the model equation (D.1). Expanding the χ^2 objective function in a Taylor series at the minimizer $\mathbf{a}_0$, the first-derivative terms drop out, because the gradient is zero, leaving the variation in χ^2 dependent on the second-derivative terms. This leaves, for any small change $\delta\mathbf{a}$ in the model parameters,

$$\Delta\chi^2 \approx \delta\mathbf{a} \cdot [\alpha] \cdot \delta\mathbf{a} \tag{D.4}$$

where matrix $[\alpha]$, defined by

$$\alpha_{kl} = \sum_{i=1}^{N} \frac{1}{\sigma_i^2} \left(\frac{\partial f(\mathbf{x}_i, \mathbf{a})}{\partial a_k} \frac{\partial f(\mathbf{x}_i, \mathbf{a})}{\partial a_l} \right) \tag{D.5}$$

is an approximation to 1/2 the Hessian (second derivative matrix) of the χ^2 objective function. As it turns out, and this will be important later, $[\alpha]^{-1}$ is the so-called covariance matrix $[C]$, calculated in the Levenberg-Marquardt Algorithm.

Now we restrict ourselves to a fixed k and a curve $\mathcal{C}$ in M-dimensional parameter space defined as the locus of the following points:

- a_k a random variable from the universe of experimental realizations, and
- the other parameters (a_l for $l \neq k$) adjusted (as a function of a_k) to minimize χ^2, which is evaluated using a fixed data set.

It turns out that the distribution of χ^2 for the points on $\mathcal{C}$ is chi-square with one degree of freedom.

Along $\mathcal{C}$, by definition, all but the k-th component of the gradient of χ^2 is zero. But the gradient of χ^2 may be written

$$\nabla\chi^2 \approx \frac{\partial^2\chi^2}{\partial a_k \partial a_l} \cdot \delta a_l = 2[\alpha] \cdot \delta \mathbf{a} \tag{D.6}$$

so that for $\delta\mathbf{a}$ tangent to $\mathcal{C}$ at the minimizer $\mathbf{a}_0$

$$[\alpha] \cdot \delta\mathbf{a} = b\delta_k \tag{D.7}$$

where δ_k is the vector with one in its k-th component and zero elsewhere and b is some constant. Substituting (D.7) into (D.4) gives

$$\Delta\chi^2 \approx \delta\mathbf{a} \cdot b\delta_k = b\,\delta a_k \tag{D.8}$$

along $\mathcal{C}$. But also, (D.7) may be solved to give

$$\delta\mathbf{a} = [\alpha]^{-1} \cdot b\delta_k = [C] \cdot b\delta_k \tag{D.9}$$

or, in particular,

$$\delta a_k = bC_{kk} \tag{D.10}$$

Eliminating b between equations (D.8) and (D.10) gives

$$\delta a_k = \sqrt{\Delta\chi^2}\sqrt{C_{kk}} \tag{D.11}$$

which holds so long as $\delta\mathbf{a}$ is tangent to $\mathcal{C}$ at $\mathbf{a}_0$.

Since we know the distribution χ^2 along $\mathcal{C}$ is chi-square with one degree of freedom we are in business. The p-confidence interval for parameter a_k may be expressed

$$\delta a_k = \pm\sqrt{\Delta_p}\sqrt{C_{kk}} \tag{D.12}$$

where Δ_p, is the number for which the probability is p that a chi-square variable with one degree of freedom is less than Δ_p. Δ_p can be found in tables for several values of p, or can be computed numerically as a function of p. For example, with 68.3 percent confidence ($p = 0.683$), $\Delta_p = 1$, with 90 percent confidence $\Delta_p = 2.71$, etc.

Equation (D.12) is readily evaluated, but we must keep in mind that its validity depends on a good fit of the model to the data. If the value χ^2_{min} found in the function minimization process is too large (unlikely) then our assumption that it is distributed as a chi-square variable with $N - M$ degrees of freedom is probably wrong. In this case our Δ_p estimate (made as above) would be underestimated and our confidence intervals would be too small.

Appendix E

Software

Data reduction is a multi-step process where hardware data is converted into final heat-transfer or pressure-drop correlations. Along the way, a number of computer files come into being. These start out with run-date encoded names and progress to more descriptive names later on. These names, and other important information, are hand recorded on log sheets for future reference.

The individual computer programs that make data reduction possible are:

Heat-Transfer Reduction

program	input	output	description
RRLSEL	interactive	console	select sample length
REGENRIG	.RR file	.RAW file	source data
RRHSCRN	.RAW file	.SCN file	data screening
RRHTRANS	.SCN file	.DRV file	data processing and translation, including numerical modeling
COMBINE	.DRV rile	.DRV file	combines files together
RRVIEW	.DRV file	.DRV file	data viewing, sorting, selecting
RRHFUDGE	.DRV file	.DRV file	data correction
RRH1, ...	.DRV file	console	data modeling

Pressure-Drop Reduction

program	input	output	description
REGENRIG	.RR file	.RAW file	source data
RRPSCRN	.RAW file	.SCN file	data screening
RRPTRANS	.SCN file	.DRV file	data processing and translation, including numerical modeling
COMBINE	.DRV rile	.DRV file	combines files together
RRVIEW	.DRV file	.DRV file	data viewing, sorting, selecting
RRPFUDGE	.DRV file	.DRV file	data correction
RRP1, ...	.DRV file	console	data modeling

Except for COMBINE, which is a DOS batch file, these programs are source-coded in Microsoft Pascal and run under MS-DOS.

The following account is a rough outline of the data reduction process. Individual programs, previous report [3] and a number of unpublished personal memoranda contain more detailed comments.

Size Sample Length Prior to testing, program RRLSEL estimates the best sample length for accurate data reduction over the broadest range of Reynolds number.

Log Data During testing, program REGENRIG logs a number of data points producing a .RR data file in binary format.

Convert to Raw Format Later, program REGENRIG reads the .RR file as input and writes a .RAW data file by the same name as output. The .RAW file has ASCII format and can be modified with a text editor to delete bad data points by hand, etc.

Screen Data Program RRPSCRN or RRHSCRN screen .RAW files, removing bad data points and performing elementary processing (such as determining static conduction q_{k0} from zero-amplitude points), producing .SCN files. Often run in batch mode on multiple files using RUNSP.BAT or RUNSH.BAT.

Simulation Program RRPTRANS or RRHTRANS read .SCN files as input, call on numerical simulation and optimization modules to duplicate the test point, producing binary .DRV files. Often run in batch mode on multiple files using RUNTP.BAT or RUNTH.BAT.

Combine Batch file COMBINE.BAT concatenates individual .DRV files into a single .DRV file, usually to combine runs with the same test sample taken on different days. Done with the DOS COPY /B command, or similar.

Select Program RRVIEW reads .DRV files enabling the user to individually view, discard and sort data points, if necessary.

Correct Programs RRPFUDGE and RRHFUDGE allow the user to modify individual fields for each data point of a .DRV file, if necessary. Often run in batch mode on multiple files using RUNFP.BAT or RUNFH.BAT.

Data Modeling Programs RRP1, RRH1, ..., read .DRV files, fitting coefficients of correlating expressions to data, producing tabular output (in file RRMODEL.OUT) and graphical output. Graphical output can be printed with a DOS screen printing utility.

Appendix F

N_u and N_k Physics

In correlations (2.6) and (2.7) we assumed that Nusselt number N_u and axial conductivity enhancement ratio N_k both scaled in proportion to Reynolds number raised to the same power. To justify this in porous flows, we can make use of the same methods developed for study of turbulent flows — namely, that enhancements over molecular thermal diffusion are understood in terms of fluctuating parts of velocity and temperature fields. In two dimensions, for example, $u = \overline{u} + u'$ and $v = \overline{v} + v'$ are the x and y velocity components and $T = \overline{T} + T'$ is temperature, the $\overline{\ }$ operator denoting the local steady part and $'$ denoting the fluctuating part. Even though flow through porous materials is not strictly turbulent, it does have small fluctuating components superimposed on the steady fluid variables and therefore can be understood in the same terms. Irregularities present in porous flow include flow separations caused by abrupt expansions, recirculations, vortex shedding, channeling and even true turbulence at high enough Reynolds numbers.

In our case of oscillating flow, the steady part of a fluid variable refers to its ensemble average in the sense of a large number of instances at the same position and crank angle. The fluctuating part is the instantaneous deviation from the steady part. But even the steady part of a flow variables is on too fine a scale to be resolved in a typical computational solution. So we will talk of yet another average value, the *mean-flow* value, which is the steady part spatially-averaged over a region comparable in size to the computational grid. Steady and fluctuating parts are denoted with overbars and primes as above. We have no special notation for mean-flow values, preferring to just state the fact in English when required.

The key phenomenon is the diffusion of thermal energy brought about by fluctuating velocity components in the presence of a temperature gradient. This occurs at a scale not resolved by the usual computational grid, hence the need for empirical notions such as enhanced axial conductivity and film heat transfer coefficient, non-dimensionally represented in terms of axial conductivity ratio N_k and Nusselt number N_u.

Chapter XXIII of Schlichting [11] shows that, for an incompressible fluid,

the enhanced heat flux per unit area passing through planes normal to the x and y directions is

$$\overline{q_x} = \rho c_p \overline{u'T'} \quad \text{(F.1)}$$

$$\overline{q_y} = \rho c_p \overline{v'T'} \quad \text{(F.2)}$$

It is easy to see that these are just those parts of standard enthalpy-flux integrals not resolved by the steady flow variables. Less clear is why velocity and temperature fluctuations should be correlated in the presence of a temperature gradient. To understand why, assume there is a steady temperature gradient, say $\frac{\partial \overline{T}}{\partial x} \neq 0$, and let your point of observation be centered on a fixed-in-space microscopic volume element on the same order of size as the smallest flow eddies. Into this volume element comes a fluid eddy perturbed from the steady velocity by amount u'. At this point it helps to think of u' as just one component of the full spectrum of velocity fluctuation, say $u' = A_\omega \cos \omega t$. Because of the temperature gradient, the eddy temperature differs from the steady temperature of the surroundings by an amount $\frac{\partial \overline{T}}{\partial x} \Delta x$, where $\Delta x = \int_t u' = (A_\omega / \omega) \sin \omega t$ is a sort of mixing length representing the present displacement of our eddy compared to the steady flow. This temperature fluctuation does not contribute to enhanced heat flux because Δx and u' are 90 degrees out of phase, canceling over time. However, it does drive a flow of heat, by molecular conduction, to or from the local surroundings, roughly $Q \propto \frac{\partial \overline{T}}{\partial x} \Delta x$, in turn producing an additional temperature fluctuation $\int_t Q \propto \frac{\partial \overline{T}}{\partial x} \int_t \Delta x \propto -\frac{\partial \overline{T}}{\partial x} (A_\omega / \omega^2) \cos \omega t$. Evidently this temperature fluctuation does correlate with u' and produces the enhanced heat flux. It is seen that enhanced heat flux is similar to a shuttle heat transfer mechanism operating between each flow eddy and its ensemble-average surroundings.

At this point we conclude that the enhanced heat flux vector at any point may be represented in the form $\mathbf{q} = k_t \nabla \overline{T}$, where k_t, the eddy conductivity, depends only on the nature of the local velocity fluctuations and $\nabla \overline{T}$ is the local steady temperature gradient. Generally we should expect that k_t varies from point to point and time to time in the porous flow field, and also varies with the direction of $\nabla \overline{T}$ at any given point. But we will get nowhere thinking like this so we will now make an assumption about k_t which will turn out to be important: we assume that k_t is a function only of the mean-flow Reynolds number R_e and that it varies with R_e in the same way at each point of the porous flow field. This would be true, for example, if k_t were everywhere proportional to R_e^a for some exponent a.

In order to talk next about enhanced axial conduction and film heat transfer, we need to introduce some notation regarding the regions within which these phenomena are taking place. In both cases we will be referring to a volume element $\mathcal{C}$ of a porous matrix — a cube aligned with the coordinate axes whose side dimension dx is much larger than the pore size of the matrix but still small compared to the computational grid, so that mean-flow variables may be considered uniform within $\mathcal{C}$. The void volume within $\mathcal{C}$ is denoted $\mathcal{V}$, with volume V. And the surface of $\mathcal{V}$, which is mainly the surface of the gas-solid interface within $\mathcal{C}$, is denoted $\mathcal{S}$, with area S.

We will also require another bold assumption: that the steady fluid temperature gradient may be decomposed everywhere into a part that drives enhanced axial conduction and a part that drives film heat transfer. In notation $\nabla\overline{T} = \nabla\overline{T}_k + \nabla\overline{T}_h$. Another way of looking at this is to suppose that the enhanced heat flux vector at every point of the flow field contributes partly to enhanced axial conduction and partly to film heat transfer. We just imagine that said decomposition exists implicitly, and is uniquely determined, not that we can expressly evaluate it.

F.1 Axial Conductivity Ratio

To best understand enhanced axial conduction, imagine our volume element $\mathcal{C}$ with fixed temperature boundary conditions imposed on the axially opposite faces so that there is a mean-flow axial temperature gradient set up. This temperature gradient will impress itself on the fluid everywhere within void volume $\mathcal{V}$, with local steady variations to some degree. These local variations may be supposed significant in some cases, but $\nabla\overline{T}_k$ should always scale in proportion to the mean-flow temperature gradient. Clearly, the previously described enhanced heat flux mechanism will be active within void volume $\mathcal{V}$ and the individual enhanced heat flux vectors will sum together into an effective mean-flow enhanced axial heat flux for the entire volume. It is this mean-flow enhanced axial heat flux, divided by that expected from molecular conduction alone, which is our dimensionless group N_k. Evidently, N_k depends only on some weighted average of k_t over $\mathcal{V}$ and with our previous assumption as to the nature of k_t, we conclude that N_k must vary with mean-flow Reynolds number in the same way as k_t does.

F.2 Nusselt Number

Relating Nusselt number to k_t is also possible. Consider again our volume element $\mathcal{C}$, this time focusing on film heat transfer. Taking first the usual macroscopic engineering point of view, the heat flow between the fluid and solid is formulated as

$$Q = hS\Delta T_f \tag{F.3}$$

where h is a film heat transfer coefficient and ΔT_f is the mean-flow to solid surface temperature difference. (Here, we have ignored that relatively-small part of $\mathcal{S}$ formed by the outside boundary of $\mathcal{V}$ that falls within the fluid.) But this same heat flow is also the surface integral over $\mathcal{S}$ of the normal heat flux, or

$$Q = \int_{\mathcal{S}} \mathbf{q}\cdot\mathbf{n}\,ds \tag{F.4}$$

where $\mathbf{n}$ is the unit surface normal vector. To get away from the surface where molecular conductivity dominates we need to translate this into a volume inte-

gral using the divergence theorem which says, in this case:

$$Q = \int_{\mathcal{V}} \nabla \cdot \mathbf{q}\, dv \tag{F.5}$$

Presuming eddy conduction dominates (otherwise we would be in the limiting range of constant $N_u = N_{u0}$), and using our above formulation for $\mathbf{q}$, we can now write

$$Q = \int_{\mathcal{V}} \nabla \cdot k_t \nabla \overline{T}_h \, dv = \int_{\mathcal{V}} \left(k_t \nabla^2 \overline{T}_h + \nabla k_t \cdot \nabla \overline{T}_h \right) \, dv \tag{F.6}$$

Equating the right sides of equations (F.3) and (F.6) allows us to solve for film coefficient h, and then Nusselt number as

$$N_u = \frac{d_h}{kS\Delta T_f} \int_{\mathcal{V}} \left(k_t \nabla^2 \overline{T}_h + \nabla k_t \cdot \nabla \overline{T}_h \right) \, dv \tag{F.7}$$

where d_h is hydraulic diameter and k is molecular conductivity. If we now make the additional assumption that $\nabla \overline{T}_h$ (and therefore $\nabla^2 \overline{T}_h$) scales everywhere in proportion to the film temperature difference ΔT_f, we conclude that Nusselt number is proportional to a weighted average over $\mathcal{V}$ of k_t and ∇k_t. If k_t varies only with R_e, then we might as well assume that ∇k_t does too, so we conclude that N_k must vary with mean-flow Reynolds number in the same way as k_t does.

F.3 Similarity

Based on the above discussion we find it arguable that both axial conductivity ratio N_k and Nusselt number N_u vary with mean-flow Reynolds number in the same way as does eddy conductivity k_t. The main simplifying assumptions leading to this conclusion were that:

- Eddy conductivity k_t is the principal phenomenon responsible for enhanced mean-flow axial conduction and film heat transfer, or at least for their variations with mean-flow Reynolds number.
- This eddy conductivity varies with mean-flow Reynolds number, the same way at all points of the flow field and in all directions.
- Local steady fluid temperature gradient may be decomposed into an enhanced axial conduction part and a film heat transfer part, the former scaling in proportion to the mean-flow axial temperature gradient and the latter in proportion to the film temperature difference.

Therefore, to the extent this is all true, we are justified in Simultaneously reducing N_k and N_u in the forms of correlations (2.6) and 2.7). Further evidence that this is a reasonable thing to do comes in the form of the relatively tight confidence intervals obtained for the resulting parameter estimates.

Bibliography

[1] Y. Bard, *Nonlinear Parameter Estimation*, Academic Press, (1974).

[2] J.E. Coppage and A.L. London, *Heat Transfer and Flow Friction Characteristics of Porous Media*, Chem. Eng. Prog., vol. 52, no. 2, pp. 57-F–63-F, (1956)

[3] D. Gedeon, G. Koester and A. Schubert, *A Test Rig for Measuring the Thermal Performance of Stirling Cycle Regenerators*, SBIR Phase I report, Sunpower Inc. NASA Lewis contract NAS3-25620, (1989)

[4] D. Gedeon and J.G. Wood, *Oscillating-Flow Regenerator Test Rig: Woven Screen and Metal Felt Results*, Ohio University Center for Stirling Technology Research, Status Report for NASA Lewis contract NAG3-1269, (1992)

[5] D. Gedeon, *GLIMPS Version 4 User's Manual*, Gedeon Associates, (1992)

[6] J.P. Holman, *Heat Transfer*, McGraw-Hill, (1976)

[7] W.M. Kays, A.L. London, *Compact Heat Exchangers, 3rd Edition*, McGraw-Hill, (1984)

[8] G. Koester, S. Howell, G. Wood, E. Miller, D. Gedeon, *Oscillating Flow Loss Test Results in Stirling Engine Heat Exchangers*, NASA Contractor Report 182288, (1990)

[9] I.F. Macdonald, M.S. El-Sayed, K. Mow and F.A.L. Dullien, *Flow through Porous Media - the Ergun Equation Revisited*, Ind. Eng. Chem. Fundam., Vol. 18, No. 3, pp. 199–208, (1979)

[10] W.H. Press, et. al., *Numerical Recipes*, Cambridge University Press, (1986).

[11] H. Schlichting, *Boundary-Layer Theory, Seventh Edition*, McGraw-Hill, (1979).

[12] J.R. Seume and T.W. Simon, *Oscillating Flow in Stirling Engine Heat Exchangers*, 21st Intersociety Energy Conversion Engineering Conference, American Chemical Society, pp. 533–538, (1986)

[13] J.G. Wood and D.R. Gedeon, *Oscillating-Flow Regenerator Test Rig: Final Report*, Ohio University Center for Stirling Technology Research, Final Report for NASA Lewis contract NAG3-1269, (1994)

REPORT DOCUMENTATION PAGE

Form Approved
OMB No. 0704-0188

1. AGENCY USE ONLY (*Leave blank*)	2. REPORT DATE	3. REPORT TYPE AND DATES COVERED
	February 1996	Final Contractor Report

4. TITLE AND SUBTITLE
Oscillating-Flow Regenerator Test Rig:
Hardware and Theory With Derived Correlations for Screens and Felts

5. FUNDING NUMBERS
WU-233-1A-1F
G-NAG3-1269

6. AUTHOR(S)
D. Gedeon and J. G. Wood

7. PERFORMING ORGANIZATION NAME(S) AND ADDRESS(ES)
Gedeon Associates
16922 South Canaan Road
Athens, Ohio 45701

8. PERFORMING ORGANIZATION REPORT NUMBER
E-10076

9. SPONSORING/MONITORING AGENCY NAME(S) AND ADDRESS(ES)
National Aeronautics and Space Administration
Lewis Research Center
Cleveland, Ohio 44135-3191

10. SPONSORING/MONITORING AGENCY REPORT NUMBER
NASA CR-198442

11. SUPPLEMENTARY NOTES
D. Gedeon, Gedeon Associates, 16922 South Canaan Road, Athens, Ohio 45701; J.G. Wood, Wood Experimental, Albany, Ohio; Project manager, Diane M. Swec-Chapman, Power Technology Division, NASA Lewis Research Center, organization code 5460, (216) 433-2309.

12a. DISTRIBUTION/AVAILABILITY STATEMENT
Unclassified - Unlimited
Subject Category 20

This publication is available from the NASA Center for Aerospace Information, (301) 621-0390.

12b. DISTRIBUTION CODE

13. ABSTRACT (*Maximum 200 words*)

A number of wire mesh and metal felt test samples, with a range of porosities, yield generic correlations for friction factor, Nusselt number, enhanced axial conduction ratio and overall heat flux ratio. This information is directed primarily toward stirling cycle regenerator modelers, but will be of use to anyone seeking to better model fluid flow through these porous materials. Behind these results lies an oscillating-flow test rig, which measures pumping dissipation and thermal energy transport in sample matrices, and several stages of data-reduction software, which correlate instantaneous values for the above dimensionless groups. Within the software, theoretical model reduces instantaneous quantities from cycle-averaged measurables using standard parameter estimation techniques.

14. SUBJECT TERMS	15. NUMBER OF PAGES
Regenerators; Oscillating-flow; Heat transfer analysis; Stirling engines	70
	16. PRICE CODE: A05

17. SECURITY CLASSIFICATION OF REPORT	18. SECURITY CLASSIFICATION OF THIS PAGE	19. SECURITY CLASSIFICATION OF ABSTRACT	20. LIMITATION OF ABSTRACT
Unclassified	Unclassified	Unclassified	

National Aeronautics and
Space Administration

Lewis Research Center
21000 Brookpark Rd.
Cleveland, OH 44135-3191